Natural off-stoichiometry causes carrier doping in half-Heusler filled tetrahedral structures

Yonggang G. Yu, Xiuwen Zhang, and Alex Zunger

Phys. Rev. B **95**, 085201 — Published 3 February 2017

DOI: 10.1103/PhysRevB.95.085201

Natural off-stoichiometry causes carrier doping in half-Heusler filled tetrahedral structures

Yonggang G. Yu*, Xiuwen Zhang, and Alex Zunger¶

University of Colorado Boulder, Renewable and Sustainable Energy Institute,

Boulder, Colorado, USA 80309

The half-Heusler Filled Tetrahedral Structures (FTS) are zinc blende-like compounds where an additional atom is filling its previously empty interstitial site. The FTS having eighteen-valence-electron per formula unit are an emerging family of functional materials, whose intrinsic doping trends underlying a wide range of electronic functionalities are yet to be understood. Interestingly, even pristine compounds without any attempt at impurity/chemical doping exhibit intriguing trends in the free carriers they exhibit. Applying the first principles theory of doping to a few prototype compounds in the $A^{IV}B^{X}C^{IV}$ and $A^{IV}B^{IX}C^{V}$ groups, we describe the key ingredients controlling the materials' propensity for both intrinsic and extrinsic doping: (a) The spontaneous deviations from 1:1:1 stoichiometry reflects predictable thermodynamic stability of specific *competing phases*. (b) Bulk ABC compounds containing 3*d* elements in the B position (ZrNiSn and ZrCoSb) are predicted to be naturally 3*d* rich. The B=3*d* interstitials are the prevailing shallow donors, whereas the potential acceptors (e.g. Zr vavancy and Sn-on-Zr antisite) are ineffective electron killers, resulting in overall uncompensated *n*-type character, even without any chemical doping. In these materials the band edges are "natural impurity bands" due to non- Daltonian off stoichiometry such as B-interstitials, not intrinsic bulk controlled states as in a perfect crystal. (c) Bulk ABC compounds containing 5*d* elements in the B position (ZrPtSn, ZrIrSb, and TaIrGe) are predicted to be naturally C-rich and A-poor. This promotes the hole-producing C-on-A antisite defects rather than B-interstitial donors. The resultant *p*-type character (without chemical doping) therein is "latent" for C= Sn and Sb, however, as the C-on-A hole-producing acceptors are rather deep and *p*-typeness is manifest only at high temperature or via impurity doping. In contrast, in TaIrGe (B= Ir, 5*d*), the prevailing hole-producing Ge-on-Ta antisite (C-on-A) is shallow, making it a real *p*-type compound. This general physical picture establishes the basic trends of carriers in this group of materials.

Keywords: half-Heusler, carrier doping, off-stoichiometry, defects, DFT theory of defects in insulators
PACS: 71.15.Mb 81.05.Hd 72.20.Jv 72.20.Pa
(Physical Review B Regular Article; Section: Semiconductors I: bulk)

* yonggang.yu@colorado.edu

¶ alex.zunger@colorado.edu

I. Introduction: The families of half-Heusler Filled-Tetrahedral Structure compounds with 18 valence electrons

Nature's most succinct ternary structures belong to the 1:1:1 equiatomic ABC compounds [1-3]. They encompass two main families (i) The eight valence-electron (octet) family [3-9] containing the groups $A^{I}B^{II}C^{V}$ (e.g. LiZnP), $A^{I}B^{III}C^{IV}$ (e.g. LiGaSi), $A^{II}B^{II}C^{IV}$ (e.g. MgSrSi), and $A^{II}B^{III}C^{III}$ (e.g. MgYGa) and (ii) The eighteen valence-electron family [10-14] that appears in a few chemical groups such as $A^{III}B^{X}C^{V}$ (e.g. ScPtSb), $A^{IV}B^{X}C^{IV}$ (e.g. ZrNiSn), $A^{IV}B^{IX}C^{V}$ (e.g. TiCoSb), and $A^{V}B^{IX}C^{IV}$ (e.g. TaIrGe [12-14]). These are 'multi-functional materials' [11], due to their capacity to host a rich variety of 3*d*, *4d*, and 5*d* transition metal elements, and because of their appearance in numerous (over 40) crystal structure types as summarized in Ref. [12], based on the Inorganic Crystal Structure Database (ICSD) [15]. The combination of structures and elements provides opportunities for tuning and designing electronic band structures, spin-orbit coupling effect, thermal and electrical conductivity, and optical transparency [10,11,14,16-19]. Some unique functionalities achievable in such compounds include thermoelectricity [20-22] (e.g. in TiNiSn and ZrCoSb), topological insulation (e.g. in ScPtBi [13]), transparent conductivity (e.g. in TaIrGe [14]), Rashba spin splitting [23], magnetism [24,25] and superconductivity (e.g. YPtBi [26]).

The ABC families became recently a testing ground for theoretical material discovery by design approach [11,12,16-19,27,28] followed by experimental validation [13,14,29,30]. There are 483 element combinations of these eighteen-electron compounds listed in Ref. [13], of which 83 were previously synthesized [15] and 400 are plausible element combinations that were never reported ('missing compounds'). Recent theoretical predictions [13] applying the first-principles materials-by-design approach [31-33] to the 483 possibilities showed that 54 of the 400 missing are predicted to be stable new compounds, 342 were predicted to be thermodynamically unstable and 4 were too close to call.

Synthesis of 17 of these predicted stable compounds was attempted; the structure determination agreed with predictions in all cases [13,14,30]. The four chemical groups involved in this study are shown in Fig. 1,where previously known vs recently predicted and subsequently synthesized cases are indicated.

A central issue common to all newly introduced electronic materials dwells on whether carrier doping can be accomplished. This issue has only been explored experimentally for just a few FTS compounds including ZrNiSn and TiCoSb [14,20,22,34-39]. The purpose of this paper is to understand the basic physical trends in self-doping (due to natural off stoichiometry) as well as some impurity doping in this family of electronic materials. Section II will highlight the main issues and summarize the key insights expanded upon in the remainder of this paper (Figs. 2-11).

II. Key issues pertaining to introduction of carriers in Filled Tetrahedral half-Heusler compounds

Two approaches are viable for introduction of free carriers into half-Heusler compounds: external chemical (impurity) doping, and natural self-doping existing in as-grown compounds due to natural off stoichiometry (intrinsic). Carrier types in ABC compounds due to impurity doping are often explained by textbook element substitution rules: substituting a host atom in solid by an impurity atom with higher (lower) valence induces *n*-type (*p*-type) conductivity. For example, Nb or Ta doping on the Zr-site, and Sb or Bi doping on the Sn-site in ZrNiSn result in *n-type* carriers, while Sc-doped ZrNiSn (on Zr-site) [40], Sn-doped ZrCoSb (on Sb-site) [41], and Fe-doped TiCoSb (Co-site) [42] are *p*-type. In contrast, natural carrier generation in pristine samples continue to bring in surprises on carrier types as well as carrier dependence on temperature, as new experimental results emerge. We will discuss intrinsic doping in Sec. IV A–C, illustrate impurity doping in Sec. IV-D, and articulate our proposed conceptual framework for doping in Sec. V. Our stoichiometry and defect computation and physical analysis (Figs.

2–11) leads to the following key perspectives on doping ABC compounds, which interpret a range of experiment and provide new insights into the problem.

A. Natural off stoichiometry is generally reflected by compound thermodynamics and controls electrical behavior*:* Unlike Daltonian compounds with strict stoichiometry, half-Heusler compounds are prone to chemical off-stoichiometry, which strongly influences their carrier and defect properties. A number of such compositions were empirically observed in the FTS phase (in the MgAgAs structure) in the past, e.g. $ZrNi_{1+x}Sn_{1-y}$ (x=6%, y=0.8%) [43], $ZrNi_{1+x}Sn$ (x=0–10%) [44], $HfNi_{1+x}Sn$ (x=0–25%) [44], $Ti_{1+x}Ni_{1+y}Sn$ (x=4%, y=3%) [36]. The theoretical question posed here is what causes off-stoichiometry and how they affect carrier doping.

While some of the off stoichiometry may be enhanced or diminished by control of metastable condition or non-equilibrium (e.g., over or under saturation of reactants), the basic trends of a given sublattice being persistently off stoichiometric in a particular direction is thermodynamically predictable. We observed an interesting phenomenon from calculations—when the B atom is a 3*d* transition metal element (e.g. ZrNiSn and ZrCoSb), the off stoichiometry is in the direction of B-*excess*, but when B is a 5*d* element (e.g. HfPtSn and TiIrSb) the off-stoichiometry is C-rich and A-poor. Such off-stoichiometry is a direct consequence of the thermodynamic competition between the host and its competing phases (discussed in Sec. III-B). Off-stoichiometry induces *preferential* defects; the latter then creates electric carriers if they can ionize at finite temperature, as will be discussed in Sec. IV and Figs. 2–7.

B. The thermodynamic preference for specific deviations from perfect stoichiometry controls specific intrinsic defect types*:* An immediate outcome of the understanding of the origin of natural off stoichiometry is that one can predict theoretically from thermodynamic stability vs chemical potentials (e.g. Fig. 3) the likely charge-neutral intrinsic defects that will abound—we will show that because the stability domain of ANiSn and ACoSb (A=Ti, Zr, and Hf) lie at the upper half of the full triangle frame

(Fig. 3), these compounds are naturally B-element rich (B=Ni or B=Co). This implies the possibility of B-interstitials and B antisite defects (B-on-A or B-on-C), and the scarcity of B vacancies. On the other hand, we will show that the stability domain of APtSn and AIrSb (A=Ti, Zr, and Hf) are mainly constrained towards the hypotenuse side of the full chemical potential triangle frame, indicating C-rich condition (C=Sn or C=Sb) and lack B-rich condition. This implies the possibility of C-on-A, C-on-B, or C interstitial defects, and the lack of B-interstitials in these groups. This is discussed in Sec. III A–B and Figs. 2–3.

C. ***Crystallographic factors such as conservation of coordination numbers contribute to the selectivity of specific intrinsic defect structures*****:** Our total-energy studies substantiate another key controlling factor: The role of conservation or violation of the original coordination number. In the ABC cubic half Heusler FTS compounds the A and C sites are fourfold coordinated, whereas the B site is eight fold coordinated (Fig.2). We find that if an intrinsic defect conserves the original coordination number (CN) (as-in A-on-C and C-on-A antisite defects with CN=4) its formation energy is rather low so the defect would be likely to form; If, on the other hand, the defect does not conserve the original coordination number (as in *B-on-A, B-on-C, as well as A-on-B, and C-on-B antisite defects*) these defects would be energetically less likely. This simple rule is discussed in Sec. III-C and Fig. 2**,** and confirmed by quantitative defect formation energy calculations shown in Fig. 6 and by charge neutral defect concentration calculation from Fig. 4.

D. Certain ABC compounds cannot be impurity doped while others can, depending on the thermodynamic driving force to spontaneously form opposing defects: How the defect system responds to external impurity doping is critical to the intended carrier generation. In general [45], intrinsic 'killer defects' can appear spontaneously and negate the intended carrier doping. For instance, deliberate introduction of electron via donor doping tends to shift the Fermi energy towards the conduction band,

but, at the same time, this will lower the formation energy required to create intrinsic 'electron killers' (acceptors) such as cation vacancies. We will show that there are no such natural killer defects for *n-type* doping in ZrNiSn and ZrCoSb, but in contrast, the *p*-type doping in ZrIrSb is opposed by Sb-on-Zr (+1) defect, rendering this compound only weakly *p*-type. This explains why certain deliberate chemical doping needs to overcome the natural tendency of the host compound to develop compensating defects. This is discussed in Sec. IV-D and illustrated in Figs. 6, 7, 8, and 11.

E. The band gap anomaly in pristine $A^{IV}B^{X}C^{IV}$ compounds and its origin. For many FTS compounds the observed band gap tends to be significantly *smaller* than what can be inferred from perfect single crystals (when they exist) or from those predicted by the density functional calculations, a surprising result given that DFT generally *underestimates* band gaps relative to experiment [46]. For example, plain LDA and GGA predict for stoichiometric ZrNiSn a band gap at ~0.5 eV, yet a most recent experimental measurement by Schmitt et al. [47] gives a band gap of 0.13 eV, in agreement with early experimental value of ~0.18 eV of Aliev et al. [48]. While the anomalously small-observed band gaps are beneficial to thermoelectric applications, understanding the origin of the anomaly has been controversial. Here we briefly note the leading literature opinions and summarize the insights on this problem gained from our calculations:

(1) A literature suggestion: band gap reduction in ABC results from C-on-A atomic exchange (e.g, Sn-Zr exchange in ZrNiSn): Aliev et al. [48] proposed on the basis of X-ray analysis an A-C exchange reaction producing a pair of antisite defects: A-on-C as well as C-on-A (for example, a pair of Sn and Zr atom exchange in ZrNiSn). This idea offered a viable path to reconcile the smaller experimental band gap relative to expectations from stoichiometric DFT prediction, because band gap reduction in ZrNiSn at small Sn/Zr exchange ratio was indeed found from DFT band structure calculations [49,50]. However, recently more accurate structure refinement from Xie et al. [43] *observed no A-C exchange,* which is

consistent with DFT total energy calculations of Larson et al. [51], who showed that such exchange would be prohibitively costly in formation energy. Thus, this exchange reaction likely does not happen, so it cannot lead to gap reduction in practice. We will show in Sec. IV and Figs. 6–7 that in general by calculating simultaneously thermodynamic stability (formation enthalpy) of defects as well as their (donor and acceptor) energy levels we can establish (a) if a defect can exist in significant concentration and (b) what is its electrical effect. *If (a) is not satisfied, (b) is a moot point.* This is the case for C-on-A atomic exchanges in FTS.

(2) A Literature suggestion: band gap reduction in ABC could result from B atom Frenkel pair formation: The work from Larson et al. [51] and Romaka et al. [44] suggested that Ni Frenkel pairs in ZrNiSn could reduce its band gap because both calculations showed metallic states when a portion of Ni atoms (>25%) migrate from the host B sublattice to the vacant site. Our study showed that the thermodynamic energy cost (2 eV per Frenkel pair) tend to exclude its existence in optically significant concentrations, as shown in the Appendix (Fig. 19). Again, calculations of the *total energy* (not just defect levels) of this sort act to validate or refute prior intuitive ideas.

(3) Calculations *on a few members of the $A^{IV}B^{X}C^{IV}$ group* show that *the origin of gap reduction in a few members of the $A^{IV}B^{X}C^{IV}$ group is the formation of impurity band in the gap due to B interstitials*. Specifically, we will show that Ni excess in off stoichiometric ZrNiSn leads to an impurity band above the original (perfect crystal) valence band maximum, while, at the same time, lowering the original conduction band due to the emergence of a 'perturbed host state' from the conduction band of the perfect crystal (see Lany et al. [52] and Kent et al. [53] for the discussion of the concept of 'perturbed host state'). Both effects, described in Sec IV-B and Fig. 5 (and in more detail in Fig. 18 in the Appendix), lead to a significant reduction of the band gap due to off stoichiometry. The type of

compounds that could show a high concentration of B interstitials is hinted by the existence of a stable full Heusler analogue AB_2C to the half Heusler compound ABC in certain cases such as $ZrNi_2Sn$ and ZrNiSn. This suggests mutual solubility at high temperatures (with details shown in Fig. 17(b) in Appendix) leading to Ni-Ni clustering, in agreement with Do et al. [54]. For high enough concentration of the B interstitial there will be gap closure and a nonmetal to metal transition. This is discussed in Sec. IV-B (Figs. 5) with details given in the Appendix (Fig 17 and 18). The concept of excess Ni atoms accumulating at the interstitial sites in ZrNiSn is consistent with the photoemission experiment by Miyamoto et al. [55], showing two types of Ni sites in pure ZrNiSn samples: the host Ni site and the interstitial Ni site. That the excess Ni can introduce electronic in-gap states in density of states for ZrNiSn was simulated from DFT [51,54], with the observed low-band-gap, semiconductor electrical behavior of $ZrNi_{1+x}Sn$ ($x < 0.1$) [22,43,47,48,55,56]. *We conclude that in these materials the band edges are "natural impurity bands" due to non-Daltonian off stoichiometry, not intrinsic bulk controlled states as in a perfect crystal.*

F. The origin of carriers in self-doped pure FTS compounds: The interesting aspect of off stoichiometry in ABC compounds is that it introduces systematically and deterministically a particular type of carrier (electrons vs. holes). In an attempt to explore novel thermoelectric materials, electrical properties of many half-Heusler compounds have been measured. The basic phenomenology noted is that *n-type* materials include ANiSn (A=Ti, Zr, Hf), ACoSb (A=Ti, Zr, Hf), whereas *p*-type compounds include APtSn (A=Zr and Hf), TaIrGe , ZrIrSb , YPtSb [57], LnPdSb (Ln=Y, Ho, Er, La, Gd) [58], and LnPdBi (Ln=Nd, Y, Dy, Ho, Er, La, Gd) [59].

The origin of *n*-type doping in the paramagnetic ZrNiSn case was speculated in a number of papers. It was suggested that a B-on-A antisite in ABC compounds would create free electrons. For example the suggestion by Romaka et al. [56] assigned the Ni-on-Zr antisite defect as electron donors in ZrNiSn. Our

calculation reveals that in ZrNiSn at any allowed chemical condition, the Ni-on-Zr defect formation energy is rather high (above 2 eV) so the concentration of this defect is significantly low (below 10^{14} cm^{-3}) and negligible in the system.

(1) ***We find that the origin of n-type carriers in undoped ABC compound with B=3d elements is ionized B atom interstitials***. This explains the *n*-type behavior in ANiSn and ACoSb (A=Ti, Zr, Hf). This finding is at first surprising because it was generally assumed that a Ni interstitial with its closed shell d^{10} configuration would be a deep donor and not capable to explain the *n*-type behavior in normal samples (ZrNiSn). We will show that in ABC compounds with B=3*d* element, the B interstitial is not a deep donor but can be ionized, rendering the pure compound *n*-type. Indeed, we find (see Fig. 5) that the *spin exchange interaction in ionized Ni interstitial (1+) in ZrNiSn splits the d band into spin up (resonant in the valence band) and spin down near the conduction band minimum, the latter spin level being effectively a shallow donor that contributes free electrons.* In ZrCoSb, the ionized Co interstitial in 1+ state is stable due to the effective d^8 configuration, where the ionized electronic state falls above the conduction band. This explains the *n*-typeness due to 3*d* interstitials. Such ionization can also produce finite local magnetic moments at a dilute defect limit (Sec. IV-B). The portion of ionized B-interstitials strongly depends on the donor transition level relative to the host CBM, calculated by the HSE [60] exchange-correlation. In ZrNiSn, the calculated carrier density lies in the range of 10^{18} to 10^{20} cm^{-3} (Fig. 9), and increase with temperature (Fig. 10), while the calculated equilibrium Ni interstitial defect content can reach a maximum of 0.6% as shown in Sec. IV and Fig. 4.

(2) We find that the origin of p-type carriers in undoped ABC compound with B=5d element is the C-on-A antisite defect. *This explains the p-type behavior in TaIrGe, ZrIrSb and APtSn (A=Zr, Hf).* Previously, the contrast between *n*-type ZrNiSn and *p*-type ZrPtSn was unexplained, and stoichiometric disorder across the Zr and Sn sublattices was proposed assuming charge neutral states, which reduces

the band gap but does not explain the origin of free holes therein [48,49]. We will elucidate the acceptor nature of the C-on-A antisite defect in this group of B= 5*d* ABC compounds, and quantifies the charge compensation scenario in some of these compounds. Our results points to a different explanation: *the negatively charged C-on-A antisite defects form spontaneously and create holes in the ABC compounds with B=5d elements at favorable chemical conditions.*

The present paper will parse in sequence the specific ingredients that leads to conclusion of *n*-type (*p*-type) self-doping in Filled Tetrahedral half-Heulser compounds, propose a useful rule to help explain the doping trend in B=3*d* and 5*d* compounds, and present in details our specific observations from this series of calculations.

III. Results: inference from pristine bulk ABC compounds on their propensity to form specific intrinsic defects

A. The compounds selected here and their structures

Our materials selection family begins with four prototype chemical groups: $A^{IV}B^{X}C^{IV}$, $A^{IV}B^{IX}C^{V}$, $A^{III}B^{X}C^{V}$, and $A^{V}B^{IX}C^{IV}$ containing 72 compounds (Fig. 1). Of these, a total of 61 are predicted to be thermodynamically stable (combining 40 previously made with 21 previously missing but predicted stable). Of the 61 stable compounds 50 are cubic non-metals (shaded in green in Fig. 1) and the remaining 11 are non-cubic structures and are metals (shaded in blue) [13]. Only the 50 non-metals are candidates for meaningful defect calculations. The $A^{V}B^{IX}C^{IV}$ group in Fig. 1 has been eliminated because of a small number of semiconducting compounds. We likewise avoid the semi-metallic $A^{III}B^{X}C^{V}$ group (C= Sb and Bi) where a majority of ternaries show band gaps below 0.5 eV (HSE results in Fig. 12 of the Appendix). Among the other semiconductor groups of ABC which are more suitable for defect calculations we focus on the ANiSn, APtSn, ACosSb, and AIrSb series (A=Ti, Zr, and Hf)

forming a natural set with both A-atom and B-atom variations. The similarity between Ti, Zr and Hf elements in their chemical bonds and in their atomic radii (Ti: 2.0 Å, Zr and Hf: 2.16 Å) suggests it suitable to choose A= Zr in the four series of compounds for an illustrative study. This leads to our final choice of four compounds for carrier doping study: ZrNiSn, ZrCoSb, ZrPtSn, and ZrIrSb, the first three being previously made compounds, and the last one being recently predicted and newly synthesized compound. Table 1 of the Appendix gives the calculated lattice constants and band gaps of the bulk compounds, which is also seen from Fig. 13 in the Appendix.

The *cubic* half- Heusler compounds are all semiconductors (see Table 1 and Fig. 12–13) and exist in the filled tetrahedral structure (FTS) with space group $F\bar{4}3m$ [3-6] (Fig. 2). In the ground state structure, the B element is the group-IX element (Co, Rh and Ir) or group-X element (Ni, Pd, and Pt) located at the eight-fold site, while the A and C elements occupy the fcc sublattice, each having four B and four vacant site as nearest neighbors (see the first three coordination shells around each site in Fig. 2). We find that swapping the two elements between the eight-fold (B-site) and four-fold site (A or C-site) in the ground state structure is energetically unfavorable, costing on average 0.7 eV per formula unit (see Fig. 14 for calculations on 50 cubic non-metal ABC compounds).

B. The chemical stability field reveals tendencies towards off-stoichiometry and identifies the leading charge-neutral defects

The formation of ABC ternary under a given set of chemical potential condition with $\Delta\mu_{A,B,C} < 0$ requires that $\Delta\mu_{\mathrm{A}} + \Delta\mu_{\mathrm{B}} + \Delta\mu_{\mathrm{C}} = \Delta H\,(\mathrm{ABC})$ where $\Delta H\,(\mathrm{ABC})$ is the compound formation energy. Projection of this equation onto the $\{\Delta\mu_{\mathrm{A}}, \Delta\mu_{\mathrm{B}}\}$ plane leads to a chemical potential triangle frame $\Delta\mu_{\mathrm{A}} + \Delta\mu_{\mathrm{B}} > \Delta H\,(\mathrm{ABC})$ with $\Delta\mu_{A,B} < 0$. Further constraints to the triangle arises from the fact that the ABC ternary is stable against decomposition or converting into its competing phases (or their linear

combinations, e.g. Ref. [61]), requiring $p\Delta\mu_A + q\Delta\mu_B + r\Delta\mu_C < \Delta H$ (any competing phases with composition p:q:r of A:B:C).

To illustrate how such *bulk calculation provides important clues about non-stoichiometry* consider the following: (i) By identifying the structural differences between the target structure (ABC) and its nearest competing phase (say AB_2C) one can determine the type of defect this competing phase will produce: here, interstitial B atom is the likely defect that accommodates the off-stoichiometry in cases where the full- Heusler AB_2C is the nearest phase to ABC in the chemical potential diagram (e.g. the first row in Fig. 3). (ii) Depending on the relative location of the ABC stability region (shaded colored area in Fig. 3) with respect to the full triangle frame, the stability fields for 12 compounds can be categorized into the B-rich (green shading) or C-rich (and A-poor, yellow shading) conditions in Fig. 3. (iii) The relative size of the allowed zone (colored region in Fig. 3) indicates the ease or difficulty to synthesize the target ABC compound. (iv)The competing phases neighboring the ABC stability region (see Fig. 3) are likely the secondary phases that could appear in the sample during growth. This is especially appropriate when the competing phase has similar structural framework as the ABC half-Heusler compound (e.g. full-Heusler AB_2C materials).

C. Validation via explicit defect calculations: Figure 4 shows our calculated concentration of the main defects (each summed over all of its charge states) as obtained from actual defect calculations in which the defect formation energy is computed for supercells containing one charged defect at the time. Details of the calculation will be further described in Sec. IV-A below. We can see from Fig. 4 that indeed in the compounds with B=3*d* element (ZrNiSn and ZrCoSb), the B-interstitials (Ni_i and Co_i) have the highest concentration at B rich conditions and in the compounds with B=5*d* element (ZrIrSb and ZrPtSn), the C-on-A antisites (Sb_{Zr} and Sn_{Zr}) are predominating defects and the C-on-B and C interstitial defects in ZrIrSb or ZrPtSn all have low concentration. Our defect calculations predict a maximum of

0.6% Ni interstitial surplus at Ni-rich condition in ZrNiSn, a maximum of 1.3% Zr deficiency (V_{Zr}) at Zr-poor and Co-poor condition in ZrCoSb (Fig. 4). The maximal Sn-on-Zr defect content reaches 3.3×10^{-5} in ZrPtSn at Sn-rich condition and 6.6×10^{-6} in ZrIrSb at Sb-rich condition. It is interesting to note that these off-stoichiometries were predicted using equilibrium chemical potential conditions within the compound stability field (Fig. 3). This validates the connection between defect-free chemical potential calculation (Fig. 3) and defect calculations (Fig. 4) in terms of identifying the leading defects in these systems due to natural off stoichiometry.

D. The symmetry of the coordination shells around lattice sites provides additional clues on the leading coordination-preserving point defects

Figure 2b shows the coordination shell structure of various sites in the FTS lattice.

1. Antisite defects of A-on-C and C-on-A are energetically likely; the B antisite defects are less likely: The A and C atoms have the same first shell local structure, namely $A[B_4,V_4](C_4)$ and $C[B_4,V_4](A_4)$, respectively, where the square and round brackets denote the first and second nearest neighbors, respectively. These crystallographic factors suggest that A-on-C and C-on-A antisite defects do not change the first shell coordination structure of the lattice. They might be candidates for low formation energy defects provided the atomic sizes are compatible. On the other hand, the B site is eight fold coordinated as in $B[A_4, C_4](V_6)$ so B-on-A, B-on-C, as well as A-on-B, and C-on-B defects would be energetically less likely because such substitutions do not conserve coordination. Our calculated formation energies discussed in Sec. IV confirm such qualitative expectations based on Fig. 2.

2. The B interstitial is likely whereas A or C interstitials are less likely*:* Figure 2 shows similarity in coordination shell structures surrounding the B-site and the vacant interstitial site denoted by "V". The ideal coordination shell structure around substitutional B is $B[A_4, C_4](V_6)$, and that around V is

$V[A_4,C_4](B_6)$. Thus, when the B atom forms an interstitial by occupying the vacant V site it will create the local structure $B[A_4,C_4](B_6)$, which retains the first neighbor shell as in the ideal substitutional B structure and perturbs only the second shell. In contrast, the shell structure surrounding substitutional A is $A[B_4,V_4](C_4)$, so if A becomes interstitial on the vacant V site it will create the $A[A_4,C_4](B_6)$ local structure distinct from the ideal local environment of substitutional A. Similarly, the ideal local environment of the substitutional C site is $C[B_4,V_4](A_4)$, so if C becomes interstitial on the V site it will again create a local environment $C[A_4,C_4](B_6)$ that differs substantially from its ideal neighboring structure. This analysis points to the propensity of B to become interstitial (if size consideration permits), whereas that of A or C interstitials would perturb the local coordination structure too much. Indeed, such qualitative chemical analysis is supported by our calculated formation energy discussed in Sec. IV. Also impressive is the nearly exact match between ideal bond lengths and the relaxed bond lengths for B interstitial and C-on-A antisite defects in the selected compounds as shown in Appendix (Fig. 20, with Ir_i being an exception).

IV. Results: defect calculations on ABC compounds

A. Outline of the salient features of the method: defect formation energy, charge transition energy, equilibrium Fermi energy and carrier concentrations

The central quantities calculated here are (i) the defect formation energies $\Delta H(D,q,\mu_\alpha,E_F)$ for various charge states q, chemical potentials μ_α and Fermi energy value E_F and (ii) the defect charge transition levels $\varepsilon(D,q|q')$ between charge states q and q'.

The formation energy, $\Delta H(D,q,\mu_\alpha,E_F)$, for defect D in charge states q depend linearly on the atomic chemical potential $\{\mu_\alpha\}$ and the position of the Fermi level E_F (computational details in Appendix). Shown in Fig. 6 are the calculated formation energies for the dominant defects in four half-Heuslers. They can be used to obtain *the charge transition levels* of a specific defect, which is defined as the

Fermi energy E_{F}^{*}, at which two charged states q and q' have equal formation energy $\Delta H(D, q, \mu_\alpha, E_{\mathrm{F}}^{*}) = \Delta H(D, q', \mu_\alpha, E_{\mathrm{F}}^{*})$. This gives ε(q/q'), the transition levels, which are shown in Fig. 6 as circles connecting two charge state lines, and in Fig. 7 as "levels" in the band gaps. The transition levels do not depend on chemical potential. This calculation incorporates structural relaxations in each charge state. Generally speaking, defect D is ineffective in producing carriers if its donor level is inside the valence band $\varepsilon(+1/0) < 0$ or if the acceptor level is inside the conduction band $\varepsilon(0/-1) > E_{\mathrm{g}}$. More computational details can be found in the Appendix.

The equilibrium Fermi level E_F^{eq} is the key to determine the defect and charge carrier concentrations. This involves a self-regulating feedback effect requiring self-consistency: Take ZrNiSn for an example (Fig. 6a): electron doping say via Ni interstitials raises the Fermi level E_{F} towards CBM, however this will decrease ΔH of hole producer ($\mathrm{V}_{\mathrm{Zr}}^{1-}$), meaning more holes will form which compensate electrons, shifting E_{F} back to lower values. This creates a negative feedback loop. Eventually the Fermi level will be pinned and further electron doping becomes impossible. In ZrNiSn, the equilibrium E_{F} (for details, see Fig. 21 in Appendix) is drastically enhanced from $E_{\mathrm{C}} - 0.22$ eV to $E_{\mathrm{C}} + 0.01$ eV at the most B-rich (i.e. Ni-rich) chemical condition, indicating strong *n*-type. For ZrPtSn, the decrease in equilibrium E_{F} is only minor, creating weak *p*-type.

Figure 6 shows the formation energy of the leading defects versus *parametric* E_{F} for dominant defects and also indicates the *equilibrium* $E_{\mathrm{F}}^{\mathrm{eq}}(T, \{\mu_\alpha\})$ (at growth condition) by a vertical arrow. For ZrNiSn and ZrCoSb, the equilibrium Fermi level is located close to CBM, demonstrating these are *n*-type materials. In ZrPtSn the Fermi level is pushed to the mid-band gap and the material only display weak *p*-type. In ZrIrSb, the $E_{\mathrm{F}}^{\mathrm{eq}}$ is pinned slightly greater than the (+1/–1) transition level of the Sb-on-Zr defect in the mid-gap, producing again weak *p*-type carriers. This is the case a single defect ($\mathrm{Sb_{Zr}}$) self-compensates and pins $E_{\mathrm{F}}^{\mathrm{eq}}$.

Defect concentration and carrier density: Figure 4 illustrates the dominant defect concentration, summed over their charge states. A detailed information on dominant defect concentrations in different charge states are shown as a function of chemical condition in Fig. 23 of the Appendix. Of particular importance is the isosurface plot of majority carrier density vs chemical condition, which reinforces the concept how chemical conditions influence pertinent defects formation which in turn controls carrier generation (Fig. 9).

The proposed carrier doping rule: The 18-valence-electron ABC compounds with B=3*d* element exhibit *n*-type carriers because of B-excess off-stoichiometry which promotes B-interstitials that ionize to form donors; while ABC compounds with B=5*d* element are prone to be *p*-type materials owing to the predominance of C-rich chemical condition which promotes C-on-A antisite defects that act as acceptors to produce holes.

We summarize in Fig. 11 our defect computational results for the dominant donors and acceptors in ZrNiSn, ZrCoSb, ZrPtSn, ZrIrSb, and TaIrGe, so that their roles in producing electric carriers can be better understood in terms of chemical conditions, defect formation energy, and transition levels (e.g. Fig. 6 and Fig. 16).

B. The Origin of *n*-type carriers in ABC compounds with B= 3*d*: ZrNiSn and ZrCoSb

1. Effect of charge neutral Ni concentration on the band gap: impurity band and the impurity-perturbed conduction band: The contrast in the electronic band structure and the projected Ni 3*d* density of states between charge neutral $ZrNi_{1+x}Sn$ with Ni excess (x=6.25%) and Ni stoichiometric (x=0) is illustrated in Fig. 5. The presence of Ni_i^0 reduces the band gap by two effects—forming localized Ni_i *d*-states above the VBM and creating perturbed host state (PHS) below CBM. The spin up

and spin down density of states of Ni_i^0 state shows full spin compensation (Fig. 5b). The major part of the t_2 states are resonant in the valence band, while a majority of *e* states form in-gap states. The PHS (the green curve in Fig. 5a) results from a split down of the Zr-*d* states at the CBM, because the Ni impurity perturbs the Zr atom coordination shell from $Zr[Ni_4,V_4]Sn_6$ (Fig. 2b) to $Zr[Ni_5,V_3]Sn_6$, forming a $ZrNi_5$ cluster. Our HSE calculation on a few dilute Ni interstitial configurations reveals that the band gap of $ZrNi_{1+x}Sn$ vanishes at x=25% as seen in Fig. 17 of the Appendix. Besides Ni interstitials, the usual band gap renormalization by temperature (an electron phonon effect) is another factor that reduces band gaps, as in In_2O_3 [62] and ZnO [63].

2. Equilibrium concentration of Ni interstitials: In thermal equilibrium, when all competing intrinsic defects and their charge states were taken into account, we find (e.g. Fig. 4a) that the Ni interstitial density reaches a maximum of 0.6% at the most Ni rich chemical condition, and drops down by three order of magnitude at the Ni poor condition. The experimentally observed 2–6% excess Ni in typical ZrNiSn samples (e.g. Ref. [47]) is most likely due to non-equilibrium growth and the presence of minor phases such as full-Heusler. The calculated excess Ni concentration (analogous to the calculated Zn concentration out of equilibrium in Perkins et al. [64] for Co_2ZnO_4) would increase when adopting out of equilibrium Ni chemical conditions.

3. Ionization of Ni interstitials—in-gap level or resonant in the conduction band and the accuracy limitations of current functionals: Having a full shell $3d^{10}$ configuration, the Ni atom at normal chemical environment may be thought to be inert having high ionization energy, thus would not act as electron donors. Our spin polarized HSE calculation shown in Fig. 5 indicates that the Ni_i^{1+} exhibits strong exchange splitting between majority and minority spin channels and the net magnetic moment is about 0.8 μ_B. Electron density analysis reveals 70% of the ionized state in Ni_i^{1+} resulting from the $x^2 - y^2$ orbital, the rest being delocalized *s* and *p* states. Due to exchange interaction, the spin-majority

density state (Fig. 5b) in Ni_i^{1+} is shifted downwards in energy and hybridize with the valence band, which explains the low formation energy of the approximate d^9 configuration of Ni_i^{1+}.

There are generally two possible types of electron donors: (i) a ***resonant*** donor whose (0/+1) charge transition level lies above CBM. Like a metal, this defect system completely ionizes upon formation and shows metallic resistivity behavior with positive $d\rho/dT$. An example is Sb-doped ZrNiSn as shown in Fig. 8 (the positive $d\rho/dT$ observed from experiment at doping level 0.5% [65]) (ii) a gap level donor state whose ionization requires activation so the carrier density increases with T. Such a system can only partially ionize and is characterized by a semiconductor behavior with a negative resistivity vs. temperature slope.

Even state of the art defect calculations to date can have an uncertainty of ~ 0.1 eV in the donor transition level in terms of exchange and correlation, and thus could spuriously switch between case (i) and case (ii) above. In particular, defect calculations on materials with small band gaps (e.g. ZrNiSn, ~0.55 eV gap) is a challenge, due to uncertainties in electronic structures associated with band edges and with defect states. The GGA calculations (Fig. 15b of the Appendix) predict a deep donor level in the gap and thus a significantly low *n*-type carrier density in ZrNiSn ($< 10^{14}$ cm^{-3} at room temperature) due to dominance of charge neutral Ni interstitials. The HSE functional (mixing 25% of exact exchange) predicts a higher ionization level for Ni interstitial, above the CBM (Fig. 6a), due to effect from enhanced Hartree-Fock exchange. However, the 25% of exact exchange is only an approximation used to eliminate self-interaction corrections, we feel that our uncertainty for the Ni (0/+1) charge transition level can be 0.1 eV, considering the effect of exchange on band gap opening and on eigenvalues of in-gap states. We therefore consider two computational scenarios allowing for 0.1 eV uncertainties, as shown by point R and L in Fig. 6a. The two scenarios lead to completely different physical behavior in temperature dependence of carrier density. In case (i) the Ni interstitial completely ionizes and its (+1/0)

transition level is above the CBM (the R point in Fig. 6a). Thus the *n*-type carrier density remains nearly constant with temperature (~1×10^{20} cm^{-3}, the dashed red line in Fig. 10). While in case (ii), the Ni interstitial (+1/0) transition level lies slightly below the CBM (e.g. E_{CBM} – 0.07 eV, the L point in Fig. 6a), the Ni interstitial only partially ionizes due to thermal excitations (~10% of Ni interstitials ionize at room temperature from simulation), therefore the carrier density increases almost linearly with temperature (the solid red line in Fig. 10). When the donor is resonant we predict a high carrier density in ZrNiSn (10^{19} cm^{-3} at room temperature). This result from case (ii) is consistent with the observed linear *T* dependence of the electrical conductivity in undoped ZrNiSn samples [43,66], so it is the preferred scenario.

4. Magnetism of ionized interstitial Ni: Ni interstitials have the potential to create magnetic moments in both fully ionized and in partially ionized case. As a magnetic impurity, the Ni interstitial possesses a localized moment of ~0.8 μ_B from the $x^2 - y^2$ $3d$ orbital. For magnetism in the dilute doping limit, it was known that doping concentration has to exceed the 3D percolation threshold for the specific lattice before the itinerary ferromagnetic properties can set in [67]. Below the percolation threshold, the magnetic impurities form small clusters and they behave like super-paramagnetic states. It could be possible to observe such phenomena in delicately controlled off-stoichiometric samples.

5. *n*-type doping in ZrCoSb: Like Ni_i, the Co_i in ZrCoSb is a shallow donor, but the ionized donor electrons originate from a delocalized wavefunction in the charge neutral state (mainly *s* and *p* character), with eigenvalue lying above the CBM. In contrast, the Pt interstitial in ZrPtSn (B=5*d*) has a deep donor transition level (+1/0) close to VBM (Fig. 7b), while Ir interstitial in ZrIrSb (B=5*d*) shows bipolar behavior with donor (+1/0) and acceptor (0/1–) levels both lying close to the middle of the band gap (Fig. 7d).

The **Co vacancy in ZrCoSb** possesses a shallow donor transition (+1/0) at $E_V + 1.1$ eV (or $E_C - 0.4$ eV, Fig. 6c, 7c). With an odd number of electrons, V_{Co}^{0} state shows a magnetic moment of 1.3 μ_B (HSE results), which is delocalized and uniformly distributed on the four tetrahedral Zr atoms that contract towards the vacancy center (see Fig. 20 in Appendix for details on bond lengths). When it ionizes, the V_{Co}^{1+} state having an even number of electrons shows no net spin moment on any atom, hence energetically more favorable. The same concept, concerning the magnetic moment vs odd number of electrons, applies to Ni vacancy, explaining why V_{Ni}^{0} wins over V_{Ni}^{1+} or V_{Ni}^{1-}, the opposite to V_{Co}^{0} case.

6. Summary of the origin of *n*-type carriers in ABC compounds with B= 3*d*: The *big picture* that emerges is that for the compounds containing 3*d* elements in the B position (ZrNiSn and ZrCoSb) the bulk solids are naturally 3*d* rich and the leading electron-producing donors are consistently the B=3*d* interstitials which have low formation energy and a shallow donor transition level (0/1+). The potential electron killers (V_{Zr}, Sn-on-Zr or Sn-on-Sb) are ineffective, having either a high formation enthalpy ('A' vacancy) or deep level (C-on-A antisite). See Fig. 11 for the conceptual summary. The absence of effective electron killers opens the door in these systems not only for off-stoichiometry doping but also for effective *impurity donor doping*. For example, we find that Sb doping in ZrNiSn readily produces a high electron carrier density (10^{20} cm^{-3} at room temperature from quench) due to the (Sb-on-Sn)$^{1+}$ defect, reflecting the absence of any strong compensating acceptor (Fig. 8).

C. The origin of *p*-type carriers in ABC compounds with B= 5d: The cases of ZrPtSn and ZrIrSb

1. Interpretation on *p*-type ZrPtSn, HfPtSn, ZrIrSb, TaIrGe, LnPdSb (Ln=Y, Ho, Er, La, Gd) and LnPdBi (Ln= Nd, Y, Dy, Ho, Er, La, Gd)

There exists sporadic experimental evidence for *p*-type half-Heuslers (mostly thermoelectric materials) such as ZrPtSn, HfPtSn, ZrIrSb, TaIrGe, YPtSb [57], LnPdSb (Ln=Y, Ho, Er, La, Gd) [58], and LnPdBi (Ln=Nd, Y, Dy, Ho, Er, La, Gd) [59], yet the origin of *p*-type carriers was unknown.

The exchange or atomic disorder between A and C sublattice sites does not introduce carriers, thus cannot be the cause. Our results points to a different explanation: *the negatively charged C-on-A antisite defects form spontaneously and create holes in the ABC compounds with B=5d elements at favorable chemical conditions.* This conclusion is reached from the following physical analysis and verified from thorough defect calculations (Figs. 6, 7, and 9):

Hole producing defects consistent with C-rich conditions: In the ABC compounds containing 5*d* elements in the B position (ZrPtSn and ZrIrSb, for instance), the bulk solids contain stability fields that are naturally C-rich and A-poor (Fig. 3), favoring C-on-A antisite defects rather than B interstitials. The other potential defects that could be accommodated by C-rich condition, such as C-interstitial and C-on-B defects, are excluded due to violation of local coordination number, thus having high formation energy. The negative charge state in C-on-A defects is critical to produce holes. The hole producers can have low formation energy: In the case of ZrPtSn, the Sn-on-Zr antisite (2−), and in the case of ZrIrSb the Sb-on Zr antisite defect (1−), and in the cases of TaIrGe the Ge-on-Ta antisite (1−) (all C-on-A defect) are the primary hole producer, *all with low formation energies*.

Potential hole killer defects: At the same time, at Sn-rich condition, all hole killer defects in ZrPtSn have high formation energy thus ineffective, including Pt_i which is a deep donor and Zr_i which is a shallow donor (Fig. 6b). In ZrPtSn and ZrIrSb, however, *the relevant acceptors are deep* (Fig. 6b, 6d and 7b, 7d). This indicates that the *p*-type character in these two compounds is *latent,* being manifest only at high temperature but insignificant at room temperature (Fig. 9). The metal vacancy (V_{Zr}) having high formation energy serves only as the secondary hole producer, even though it is a shallow acceptor.

In contrast, while TaIrGe [14] also has low formation energy for the hole producer Ge-on-Ta antisite, the acceptor level is shallow (Fig. 16 of the Appendix), so this system is a *p*-type not a latent *p*-type. As a result, TaIrGe shows relatively high *p*-type carrier concentration at room temperature after quench from growth (experimental value: 0.8×10^{15} cm^{-3}, see Fig. 4b in Ref. [14]).

In addition, there are no effective donors to kill holes, since (a) the B-rich chemical condition is not available to support B interstitial and (b) the B atom is rather large so the B interstitial (Pt_i and Ir_i) becomes energetically unfavorable. As expected from the symmetry discussion in Sec. III-B, Zr_i has also high ΔH, thus will not introduce carriers even though its transition level can be shallow. Thus, there is no effective electron producers/hole killers.

2. A single bipolar Sb-on-Zr antisite defect: A very special case is ZrIrSb, an ABC compound with B=5*d* Ir element, where charged carrier compensation occurs mainly due to a single bipolar Sb-on-Zr antisite defect (Figs. 6 and 7), which is capable of acting as both acceptor (–1) and donor (+1). The charge transition level (+1/–1) lies in the middle of the band gap but closer to VBM. Since all hole-killer defects (electron donors) have high formation energy, e.g. Ir_i and Zr_i, it is the Sb-on-Zr defect itself that determines the net hole concentration. The equilibrium Fermi level is pinned slightly above the (+1/–1) transition level, which is in the mid band gap. Hence ZrIrSb can be regarded as a latent *p*-type compound, in which the hole carrier concentration is high at growth condition (e.g. 850 °C), but low at room temperature (Fig. 9).

3. Summary of origin for *p*-type carriers in B=5*d* elements in ABC compounds

The *big picture* that emerges is that for the ABC compounds containing 5*d* elements in the B position (e.g. ZrPtSn and ZrIrSb), the bulk solids contain stability fields that are naturally C rich and A poor, favoring C-on-A antisite defects rather than B interstitials. The C-on-A antisite defects are prone to form acceptors (producing holes), which can be rationalized by the strong electron negativity of IVA and VA

elements (e.g. Sn and Sb) vs the weak electron negativity group of IIIB, IVB and VB group (e.g. Y, Zr, Ta). Furthermore, shallow donors, such as B-interstitials and A-interstitials, become energetically unfavorable at the preferred chemical conditions (C-rich). Hence, no prevalent electron producers exist to kill holes.

D. Impurity chemical doping in B= 3*d* ABC compounds

Sb-doped ZrNiSn (*n*-type): Note that when we study impurity doping by Sb-doped ZrNiSn we find shallow donor states with the (0/1+) ionization level lying above the CBM as shown from the HSE calculation (Fig. 8). This is a resonant donor case with predominantly low formation energy. The absence of any effective electron killer in ZrNiSn also benefits the *n*-type behavior. Experiments illustrate metallic behavior in the Sb-doped ZrNiSn samples (Sb: at 0.5%) with the usual positive dρ/dT relationship [43], which is consistent with this calculation.

In the **Sn-doped ZrCoSb (*p*-type)**, HSE results show that Sn-on-Sb is the dominant defect having the lowest formation energy but its acceptor transition level (0/1–) is rather deep (Fig. 8). Hence the resulting hole concentration is low at room temperature and relatively high only at growth condition, 850 °C. This case illustrates a *latent p-type compound*, dominated by an uncompensated, deep, hole-producer with low formation energy (Sn-on-Sb antisite defect) which can only generate small amount of hole carriers at room temperature (see the carrier density vs. chemical condition relation in Fig. 22 of the Appendix).

E. Effect of A atom selection in ABC compounds with either B=3*d* or B=5*d* elements (the IV-X-IV and IV-IX-V groups)

Although we expect an approximately similar carrier doping behavior in the group of $A^{IV}NiSn$, $A^{IV}PtSn$, $A^{IV}CoSb$ and $A^{IV}IrSb$ compounds with A^{IV}=Ti and with A^{IV}=Zr group, we are aware of the difference among the two groups. The chemical stability field of the A^{IV}=Ti group as shown in the first column of Fig. 3 appears to be larger in area and more extended to the A-rich condition than its A^{IV}=Zr and Hf counter parts. Recently Wambach et al. [36] measured the thermopower factor in the Ti-Ni-Sn compositional space using thin film growth technique with combinatorial approach. Three major off-stoichiometry were observed in the thin film system which might have shown metastable characters: Ni-surplus in TiNiSn + $TiNi_2Sn$ assemblage, Ti-surplus and Ni-surplus in TiNiSn + Ti_2Ni_2Sn aggregate, and Sn-surplus in TiNiSn+ Sn two phase region. This is consistent with our chemical potential diagram (Fig. 2), where the stability field of TiNiSn is constrained by the Heusler phase $TiNi_2Sn$ in the Ni rich condition and Ti_2Ni at the Ti-rich condition. The stability field of Ti_2Ni_2Sn phase is nearly touching the boundary of TiNiSn at the Ti-rich and Ni-rich condition. Note the errors in the defect calculations of Wambach et al.—the full Heusler phase ($TiNi_2Sn$) is missing in the chemical stability field which contradicts experiment, and defects with the charge neutral and acceptor states (negative charge) were not included in their calculation, which would lead to inaccurate results on carrier density and defect concentrations.

F. Defect and carrier density study: the effects of chemical condition, growth and quench temperatures

To simulate carrier concentrations in samples at quenched temperature after growth or prolonged annealing (e.g. at 850 °C), we assume that the atomic local structures associated with defects are frozen in at high *T* growth condition while ionization states of defects and free carriers re-equilibrate at low temperature to preserve the charge neutrality condition. When applying this method to study variation of

carrier density with chemical condition (Fig. 9) and temperature (*T* at quench from growth as in Fig. 10**)**, we find that for ZrNiSn and ZrCoSb:

(i**) The *n*-type** carrier concentration exhibits maximum at B-rich chemical conditions (Ni-rich and Co-rich, respectively, Fig. 9), consistent with the observed coexisting Ni and Co metal phase in experiment.

(ii) The carrier concentration we obtained (~10^{19} cm^{-3}) at room temperature (quench) agrees with experiments (~8×10^{19} cm^{-3} for ZrNiSn [43] and 5×10^{19} cm^{-3} in ZrCoSb [68], shown in Fig. 10). In ZrNiSn (Fig. 9a and 9b), the *electron* concentration varies strongly with Ni chemical potential (*y*-axis) but is insensitive to Zr chemical condition (*x*-axis). This creates the horizontal stripe feature in the two-dimensional isosurface, which is due to the negligible contribution to carriers from Zr-related defects, such as V_{Zr}, Zr_i, Sn_{Zr} in ZrNiSn. Similar situation occurs in ZrCoSb (Figs. 9e and 9f), except having a weaker correlation between B-rich chemical condition and the stripe feature, which apparently is due to competition from other energetic defects, such as V_{Zr}, V_{Co} and Co_{Zr}.

(iii) Once quenched from the growth condition (850 °C), the electron carrier concentration remains high, and has only mild dependence on temperature in ZrNiSn and ZrCoSb as shown in Fig. 10. This persistent concentration vs temperature effect is the outcome of one single charged defect (B-interstitial 1+) dominating the carrier generation. Examples are Ni_i^{1+}in ZrNiSn, Co_i^{1+} in ZrCoSb (Fig. 5), and Ge_{Ta}^{1-} in TaIrGe.

In ZrPtSn and ZrIrSb, due to latent *p*-type defects (Sn-on-Zr in ZrPtSn and Sb-on-Zr in ZrIrSb), the maximal hole concentration reaches 10^{17}–10^{18} cm^{-3} at growth condition (Fig. 9e and 9g). Upon quench to room temperature, the isosurface map as a function of chemical condition shows non-linear features, indicating existence of competing *p*-type defects, while the maximum carrier density plunges to 10^{12} cm^{-3} in both compounds (Fig. 9d and 9h). The carrier density at C-rich condition shows exponential decay

with quench temperature as shown in Fig. 10. In experiment, a medium hole concentration (1.2×10^{17} cm^{-3}) is found in ZrPtSn samples where the source of defect is unknown and the Zr:Pt:Sn ratio drifts away from 1:1:1 [69]. ZrIrSb, which was recently synthesized from experiment [13], has a Seebeck coefficient (44.3 μV/K) much lower than the TaIrGe sample [14] (82 μV/K) with low hole concentration of 0.8×10^{15} cm^{-3}, and a conductivity (6.5 S/cm) much higher than TaIrGe (0.35 S/cm) [14]. Thus ZrIrSb may also have low hole concentration and high hole mobility, which however, is not given in experiment [13].

Further defect concentration analysis (see details in Fig. 23 from Appendix) reveals that in ZrPtSn when the chemical potential condition varies from Sn-rich to Sn-poor condition at growth condition (along the line R–P in Fig. 9), the amount of Sn-on-Zr acceptor defect falls off exponentially while the amount of V_{Pt}^{-1} grows up and leads to low hole concentration at Sn-poor condition. Similarly in ZrIrSb, when the chemical condition varies from Sb-rich to Sb-poor condition, the leading charged defect changes from Sb_{Zr}^{1-} to Zr_{Sb}^{1-} (Fig. 23d in Appendix). Once again, this emphasizes the role of chemical potential condition (or off-stoichiometry) on formation of intrinsic (charged) defects in half-Heusler compounds as discussed in Sec. III.

Comparing the majority carrier concentrations at growth condition (850 °C, Fig. 9 (a, c, e, g)) with those from quench (Fig. 9 (b, d, f, h)) for the four ABC compounds, we find that when a single ionized defect dominates carrier production (Ni_i^{1+} in ZrNiSn and Co_i^{1+} in ZrCoSb), quench to low temperature has only minor effects: reducing maximal carrier concentration by ~10 fold and broadening the high carrier concentration regime (n v.s. $\{\Delta\mu_\alpha\}$ plot) under chemical potential domains that favor donor formation. In contrast, the low concentration and the complex topographic feature (Fig. 9) of the quenched carriers in ZrIrSb and ZrPtSn is due to multiple competing defects: such as Sb-on-Zr (1+) versus (1–) in ZrIrSb; Sn-on-Zr (2–, 0), and V_{Pt} (1–) in ZrPtSn (Fig. 6).

V. Summary of the conceptual framework and its broad applicability

We uncover novel fundamental trends in the science of carrier doping in half-Heusler FTS compounds $A^{IV}B^{X}C^{IV}$ and $A^{IV}B^{IX}C^{V}$:

(1) Chemical potential diagram can infer the propensity for natural off-stoichiometry in the bulk compound; the latter in conjunction with crystal symmetry characteristics can promote preferential defects and suppress unfavorable ones.

(2) There are four prototype intrinsic doping cases for the $A^{IV}B^{X}C^{IV}$ and $A^{IV}B^{IX}C^{V}$ groups: (a) high *n*-type due to shallow donors while killer acceptors are of high energy. Examples: intrinsic ZrNiSn and ZrCoSb, and Sb-doped ZrNiSn; (b) latent *p*-type due to deep acceptor with low formation energy while killer donors are of high energy. Examples: ZrPtSn, and ZrCoSb:Sn; (c) latent *p*-type due to a single bipolar defect while killer donors are at high energy, example: ZrIrSb; (d) Good *p*-type due to relative shallow acceptor while killer donors at high energy, example: TaIrGe.

(3) The critical importance of understanding-based design principles for doping compounds is clearly revealed. The conceptual design scheme presented here includes the following steps: (i) identify characteristics in chemical stability fields and natural off-stoichiometry; (ii) use crystal symmetry analysis and off-stoichiometry to infer dominant charge neutral defects and verify by defect study; (iii) deduce defect compensation scenarios by inspecting ionization levels of all existing defects and their formation energy at all possible chemical potential conditions; (iv) compute carrier density at growth and quench condition throughout the allowed chemical stability field to compare with experiments; (v) compute the charged defect density in the system to verify the defect compensation scenarios. We feel that these conceptual steps have a broad validity for future defect and carrier-doping studies in various

functional materials and for comparison with experiments. Following such design approach will bring on a more comparable level the theoretical study with experimental results.

ACKNOWLEDGEMENTS

The work of YGY, XZ and AZ at CU Boulder was funded by U.S. Department of Energy, Theoretical Condensed Matter Physics, Materials Sciences and Engineering Division, Office of Basic Energy Sciences under Contract No. DE-FG02-13ER46959 to CU. This work used resources of the National Energy Research Scientific Computing Center, which is supported by the Office of Science of the U.S. Department of Energy under Contract No. DE-AC02-05CH11231. We wish to thank Jeffrey Snyder for important discussions on experiments, and Yoshisato Kimura for discussion on experiment of ZrPtSn, Giancarlo Trimarchi for helpful assistance in supercomputer work, and Liping Yu for discussion on defect calculations.

* yonggang.yu@colorado.edu

¶ alex.zunger@colorado.edu

Y. G. Yu present address: Cooperative Institute for Research in Environmental Sciences, University of Colorado, Boulder, 80309

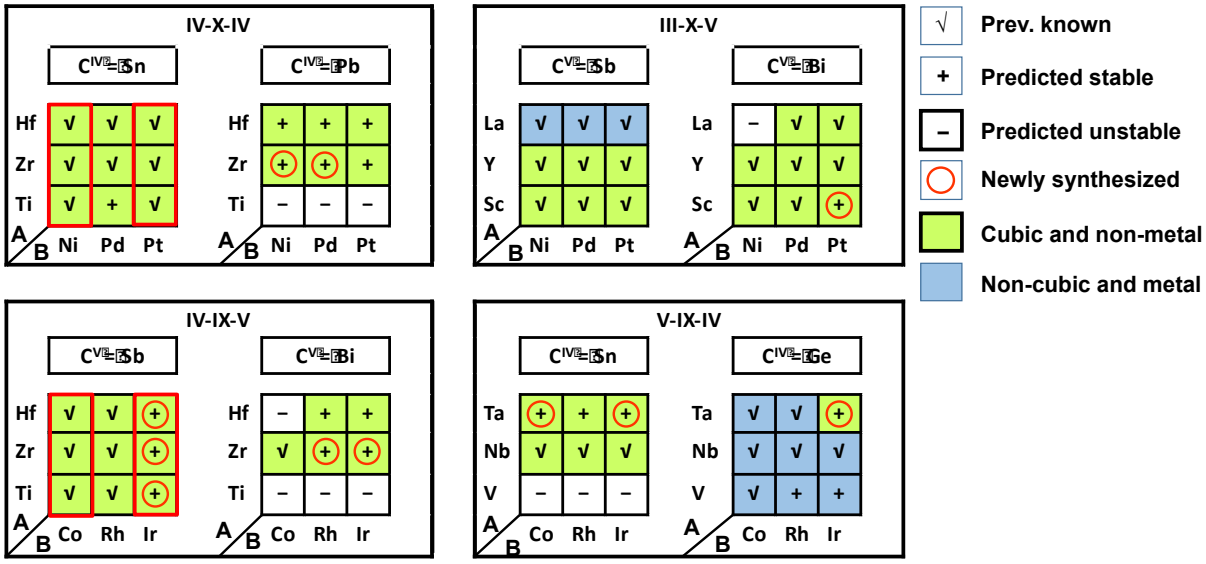

FIG. 1. Four of the existing chemical groups of the eighteen-electron ABC ternary materials containing 72 possible compounds, of which 40 are previously synthesized known compounds (denoted by √ sign). Of the 32 unreported 21 are now predicted stable (denoted by + sign) and 11 are predicted unstable (denoted by − sign). Of the 21 newly predicted compounds, 11 were recently attempted and successfully synthesized in the predicted structure [13] (shown in red circles). The ternary compounds with cubic space group $F\bar{4}3m$ are non-metals (shaded green) whereas the non-cubic compounds are metal (shaded blue). Their band gaps from hybrid functional calculations are shown in Fig. 12 (Appendix). Red circles denote recently synthesized compounds [13], and red rectangles denote a subset of $A^{IV}BC$ cubic semiconducting compounds whose carrier doping properties may be representative to this family.

(a)

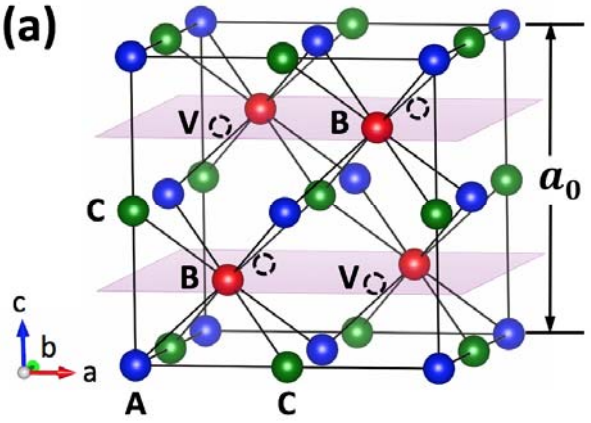

(b)

site	1st n.n. $d=\frac{\sqrt{3}}{4}a_0$	2nd n.n. $d=\frac{1}{2}a_0$	3rd n.n. $d=\frac{\sqrt{2}}{2}a_0$
A	B_4, V_4	C_6	A_{12}
B	A_4, C_4	V_6	B_{12}
C	B_4, V_4	A_6	C_{12}
V	A_4, C_4	B_6	V_{12}

FIG. 2. (a) Illustration of the four crystallographic sites in cubic Filled Tetrahedral structures with T_d symmetry (A-site, B-site, C-site, and Vacant-site). (b) Atomic identity and bond distances of the first three nearest neighbor coordination shells around each site.

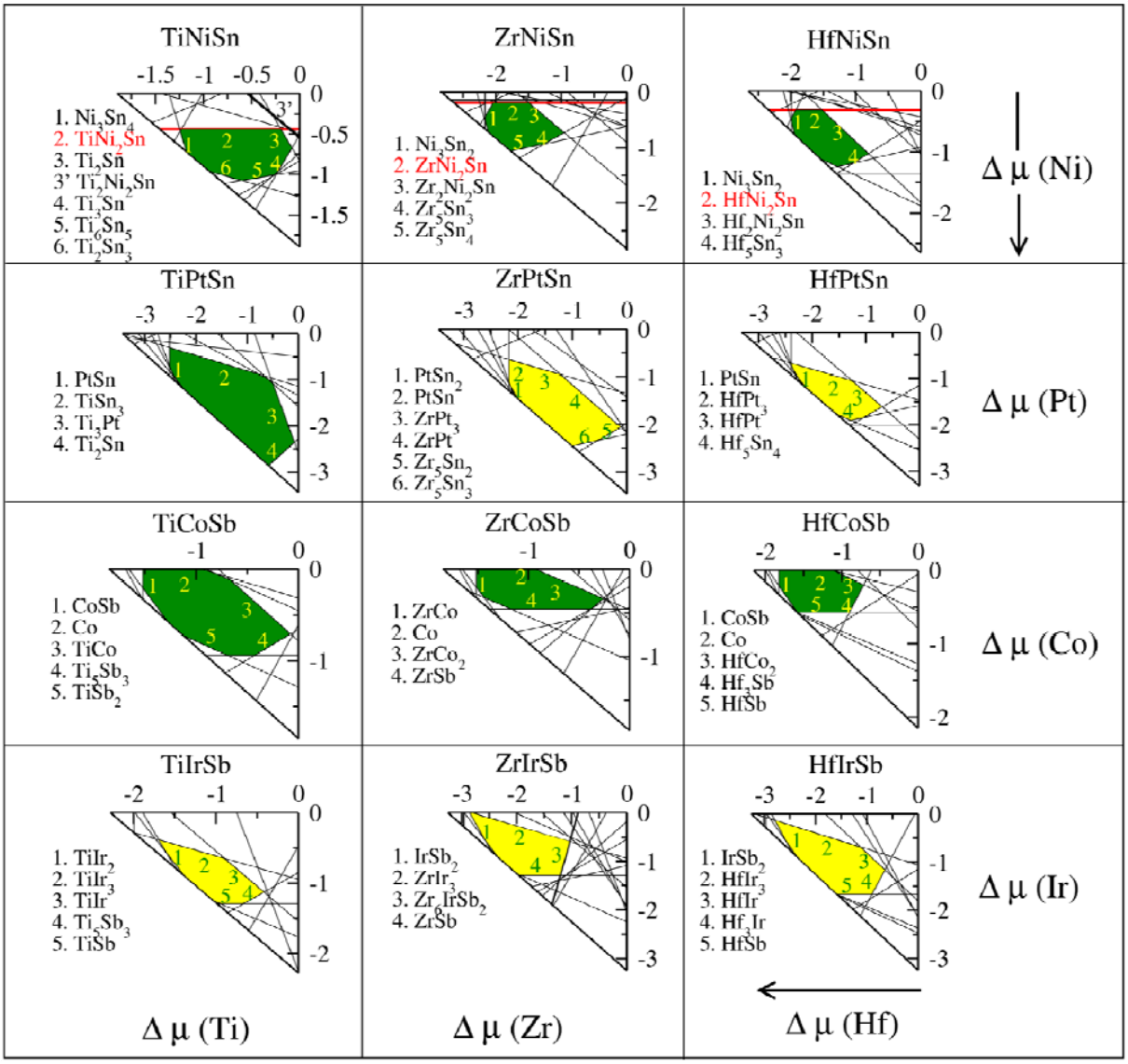

FIG. 3. The allowed chemical potential regions (green and yellow) in the versus plane of twelve cubic semiconducting $A^{IV}BC$ compounds, indicating also some of the phases competing with the stability of the ABC structure. A full list of competing phases is given in the Appendix. The green and yellow shadings serve as guide to eye for B-element rich and C-element rich chemical conditions, respectively. The chemical stability fields of the 3*d*-containing $A^{IV}NiSn$ and $A^{IV}CoSb$ (A^{IV}=Ti, Zr, and Hf) lie mainly at the upper half of the triangle axis frame indicating B-element rich conditions (Ni or Co rich), while the stability fields of the 5*d*-containing $A^{IV}PtSn$ and $A^{IV}IrSb$ are mainly constrained towards the hypotenuse side of the triangle axis frame, indicating C-element rich (Sn or Sb rich). TiPtSn has a relatively large chemical stability field, which contains both B-rich and C-rich stability field regime, and we tentatively associate it with the green color group (B-rich).

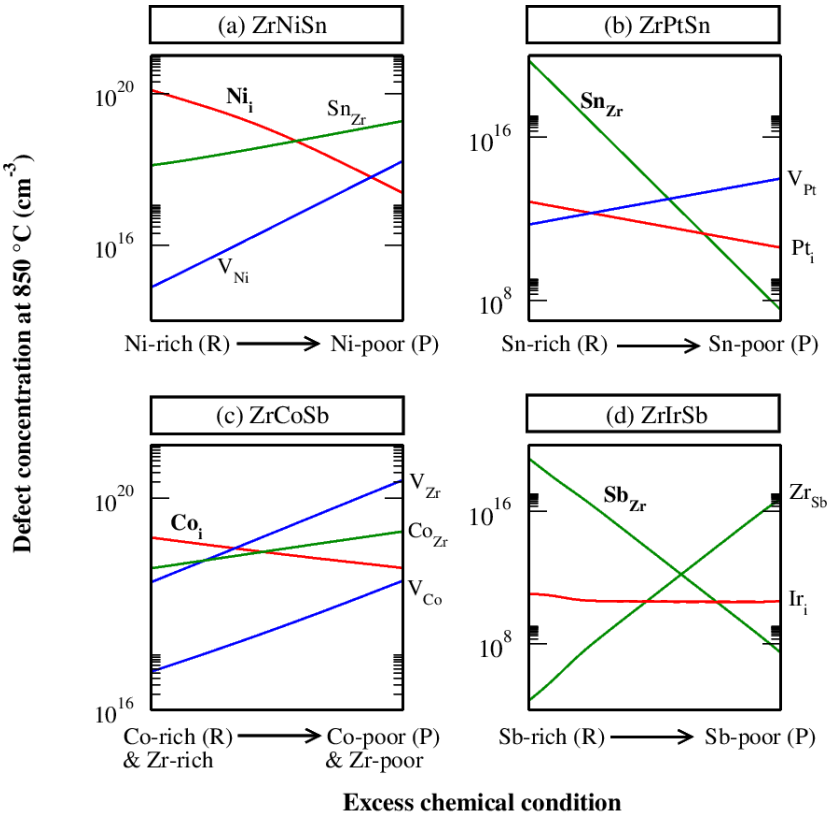

FIG. 4. The concentration of the dominant defects (each summed over all of its charged states) varying with the chemical growth condition along the line R–P in Fig. 9 at T_g=850 °C. The red, blue, and green colors denote interstitial, vacancy, and antisite defects, respectively.

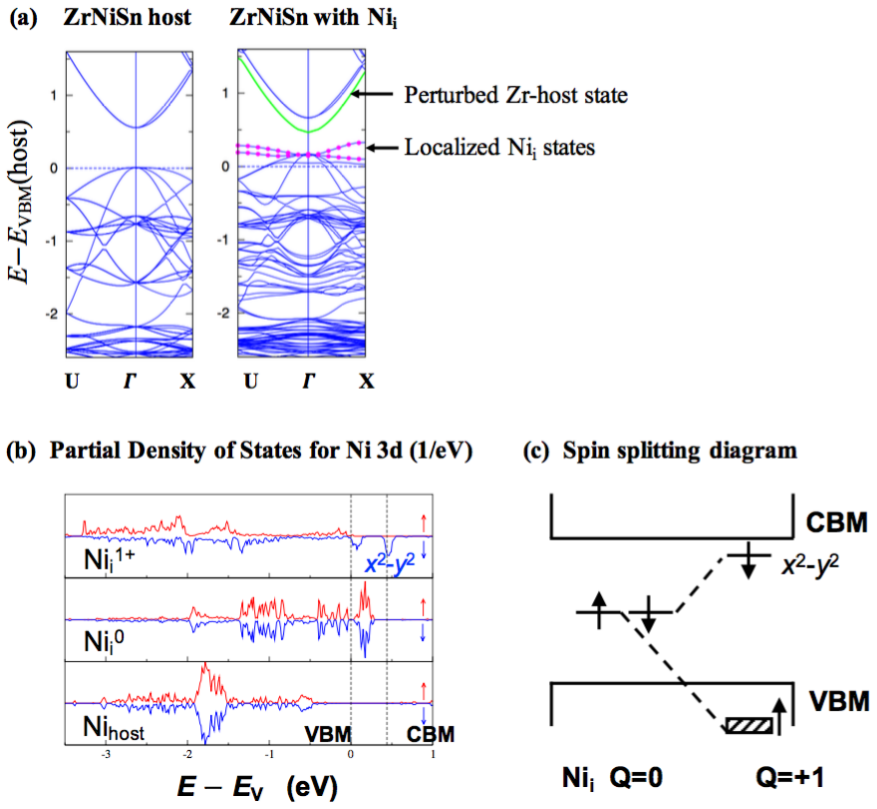

FIG. 5. (a) Electronic band structure of defect-free ZrNiSn supercell (48-atom) compared with the supercell containing one Ni_i impurity (49-atom) calculated by the HSE functional in a BCC-type unit cell: U=(1/2,1/2,1/2) and X=(1/2,0,0). (b) The projected partial density of states (PDOS) from Ni 3*d* states in a 49-atom supercell containing one Ni_i impurity in 1+ and neutral charge state compared with PDOS in the defect-free supercell (48-atom). Red and blue denote opposite spin states. (c) A schematic illustration of eigenvalues for the spin-up and spin-down HOMO states in a supercell containing one impurity (Q=0), and the spin splitting scheme in the impurity state (Q=+1).

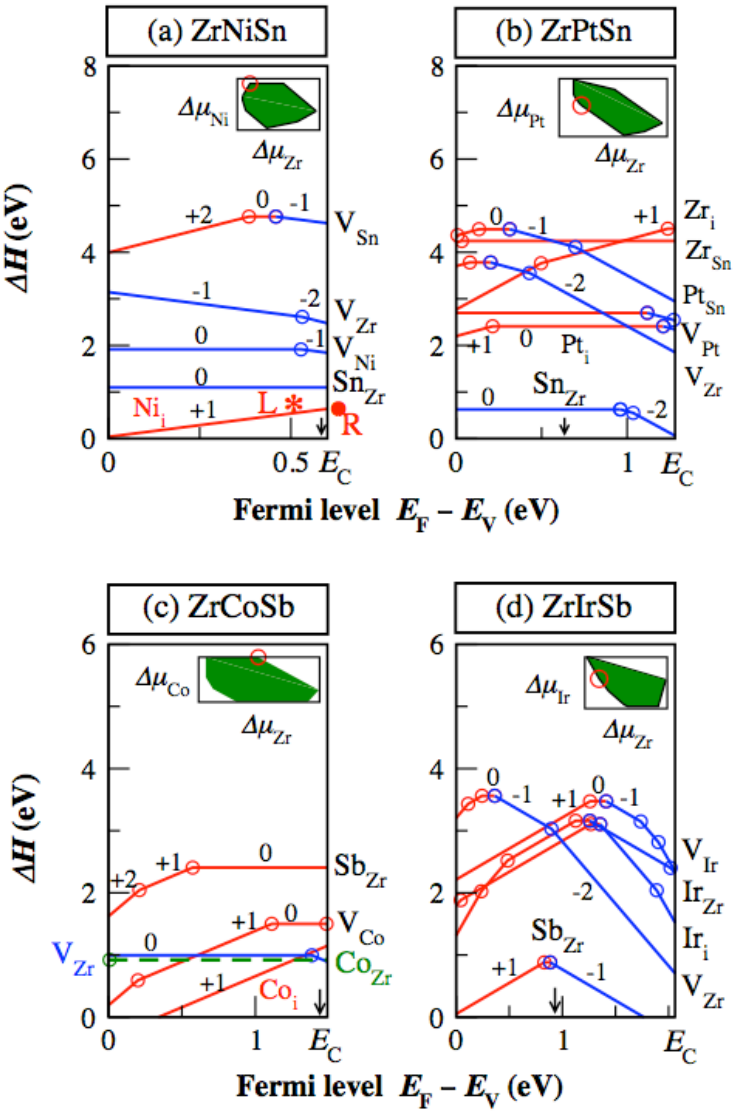

FIG. 6. Formation energy (Eq. 1 in Appendix) of the dominant defects versus parametric Fermi level in representative IV-X-IV (ZrNiSn and ZrPtSn) and IV-IX-V (ZrCoSb and ZrIrSb) half-Heusler FTS compounds from hybrid functional calculations. The main panel: positively charged electron-donor defects shown in red, negatively charged electron-acceptor defects shown in blue, their charge states denoted in numbers, and their charge transition levels shown in open circles. The Fermi level, VBM, and CBM variables are denoted by E_F, E_V, and E_C respectively. The inset shows the allowed chemical stability fields (green zones from Fig. 3), whereas the red circle shows the specific chemical condition used for v.s. E_F calculations. The small vertical arrows indicate the position of the equilibrium Fermi level at growth condition (T_g=850 °C).

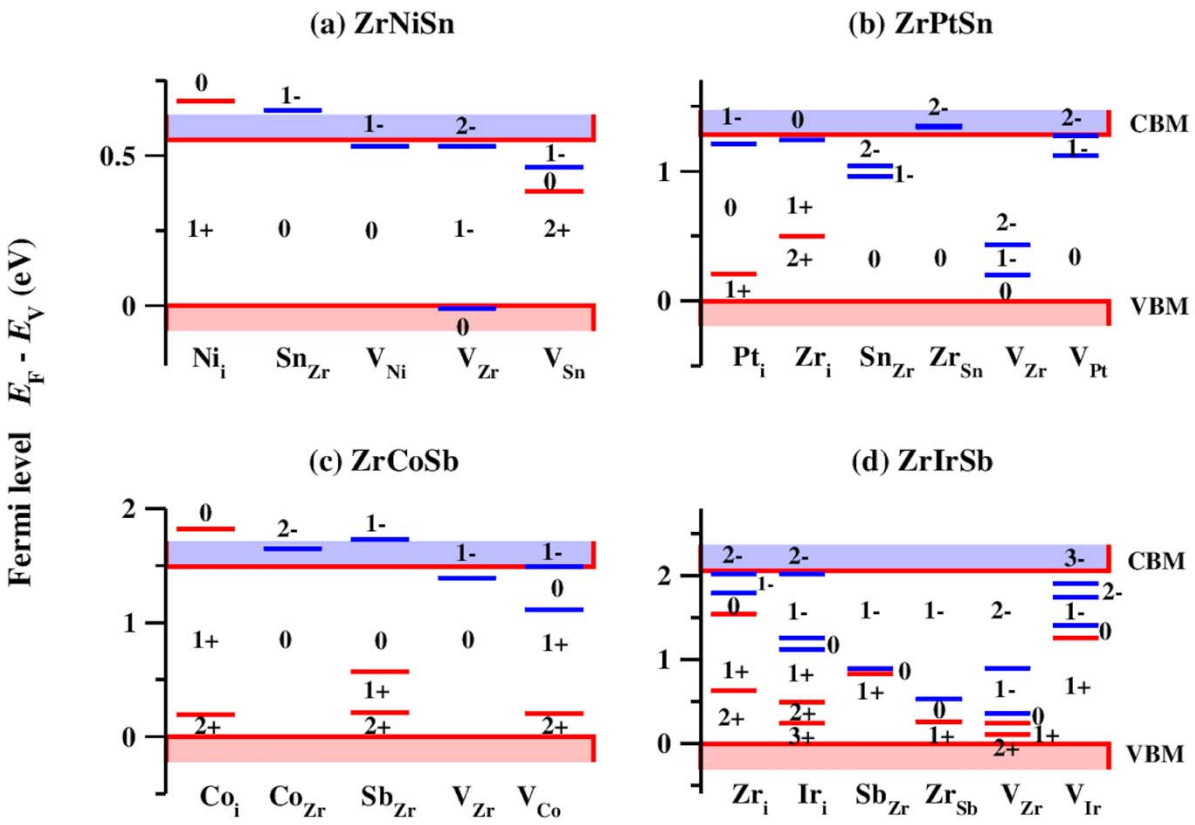

FIG. 7. Charge transition levels (Eq. 2 in Appendix) of the dominant intrinsic defects in representative IV-X-IV (ZrNiSn and ZrPtSn) and IV-IX-V (ZrCoSb and ZrIrSb) half-Heusler FTS compounds. The donor transition levels are shown in red, and the acceptor levels in blue. The red and blue shadings represent valence and conduction bands, respectively. Shallow donors are those red lines whose (+1/0) transition levels lie above or near E_C (e.g. Ni_i and Co_i), while shallow acceptors are those blue lines with (0/−1) transition level close to E_V (e.g. V_{Zr} in ZrNiSn).

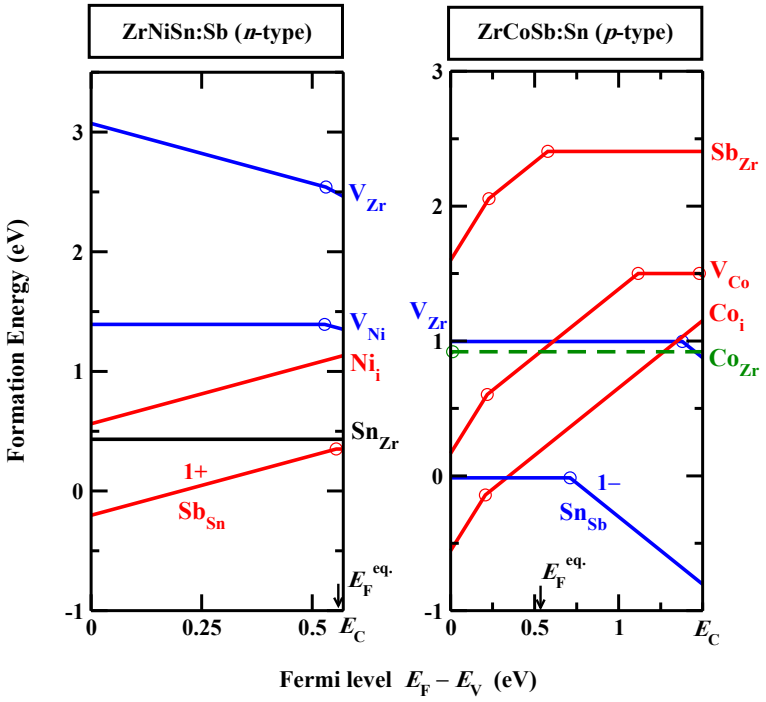

FIG. 8. Formation energy of dominant defects in (a) Sb-doped ZrNiSn at Sb-rich and Ni-poor condition (left panel), and (b) Sn-doped ZrCoSb at Sn-rich and Co-rich condition (right panel) from HSE calculations in a 48-atom supercell. The equilibrium Fermi level at growth condition (T_g=850 °C) is indicated by arrows.

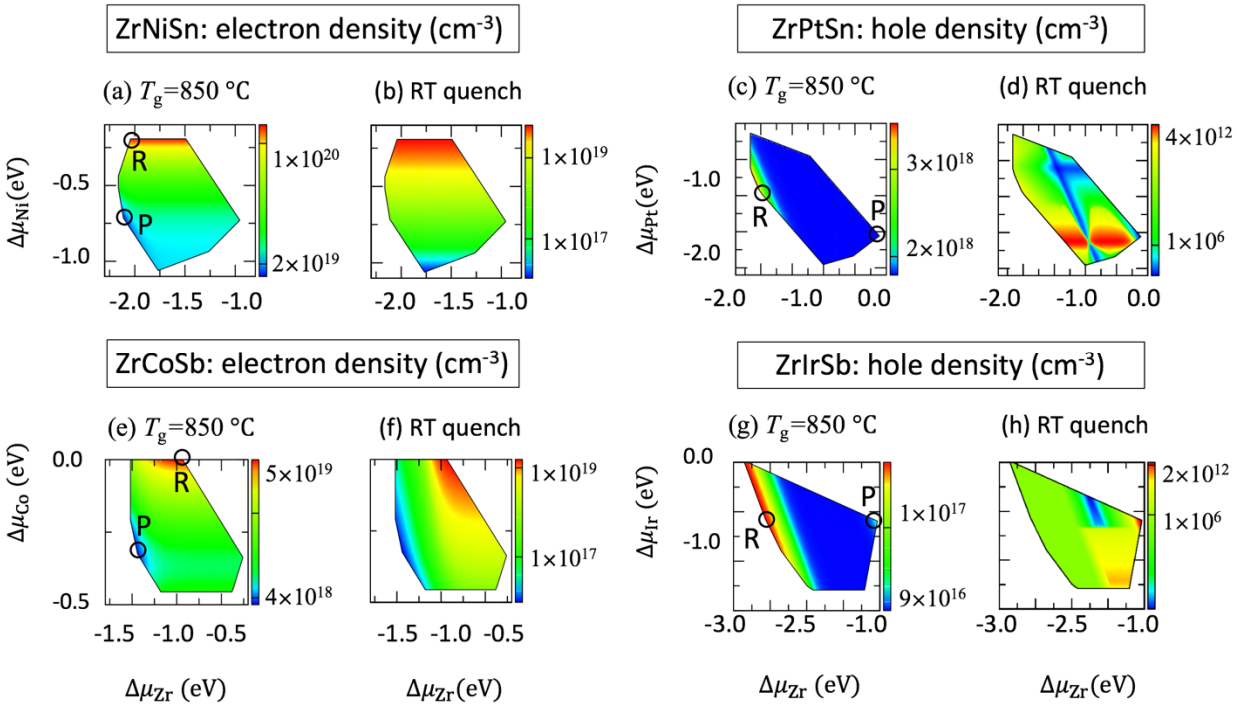

FIG. 9. Isosurface plot of the majority carrier concentrations as a function of excess chemical potentials of A and B elements within the allowed stability triangle region for four half-Haussler compounds: ZrNiSn (a,b), ZrPtSn (c,d), ZrCoSb (e,f), and ZrIrSb (g, h). The results are shown at two temperatures: at growth condition (T_g=850°C) and at room temperature from quench after growth. The letter R and P denote the chemical potential condition where high and low majority carrier concentration occurs, respectively. R and P represent, respectively, B-rich and B-poor condition for B=3*d* compounds—ZrNiSn and ZrCoSb; C-rich and C-poor conditions for B=5*d* compounds—ZrPtSn and ZrIrSb.

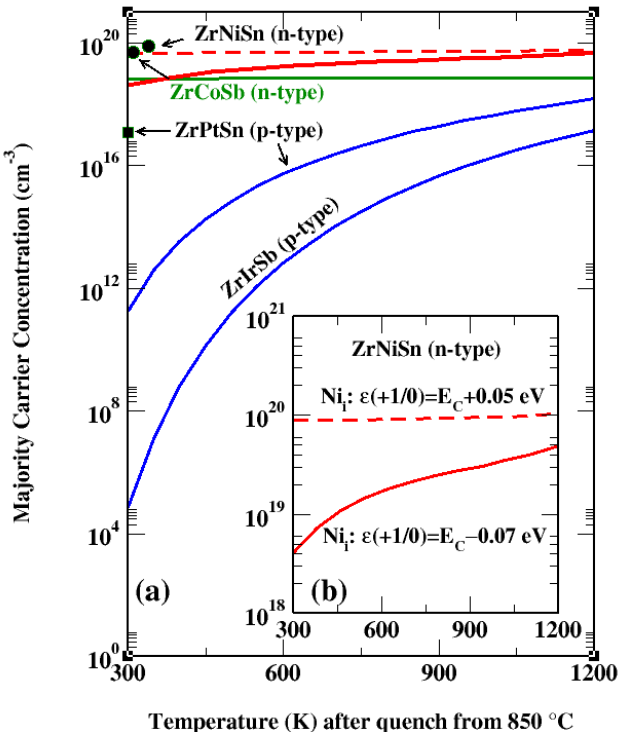

FIG. 10. (a) Majority carrier density v.s. quench temperature after growth from 850 °C for the *n*-type and *p*-type $A^{IV}BC$ compounds at B-rich and C-rich chemical conditions, respectively. The black dots denote experimental measured values for ZrNiSn [43], ZrCoSb [68], and ZrPtSn [69]. For ZrNiSn, the solid red and dashed red curves represent calculations based on two scenarios exemplified in the inset figure. (b) The *n*-type carrier density in ZrNiSn calculated from two scenarios — (i) Ni interstitial being fully ionized, the ionized state being a resonant state in the conduction band as shown from point R in Fig. 6(a). This leads to a nearly constant carrier density vs. *T* as shown in the dashed red line. (ii) Ni interstitial being partially ionized, with the ionized state staying within the band gap as shown from point L in Fig. 6(a). This leads to a sublinear relation between carrier density vs. *T* as shown in the solid red curve, which is consistent with the negative d /d*T* observed from experiments (e.g. [43,66]). In general, the quench temperature has little effect on *n*-type carriers but strong effect on *p*-type carriers. This is because in *n*-type $A^{IV}BC$, carrier-producing charged defects (B-interstitial 1+) dominate all other charged defects, while in the *p*-type $A^{IV}BC$, there is strong competition between the carrier producing charge states (C-on-A antisite *q*=) and others, e.g. C-on-A antisite (*q*=0 and 1+) charge states in ZrIrSb and B-interstitial (*q*=1+) in ZrPtSn.

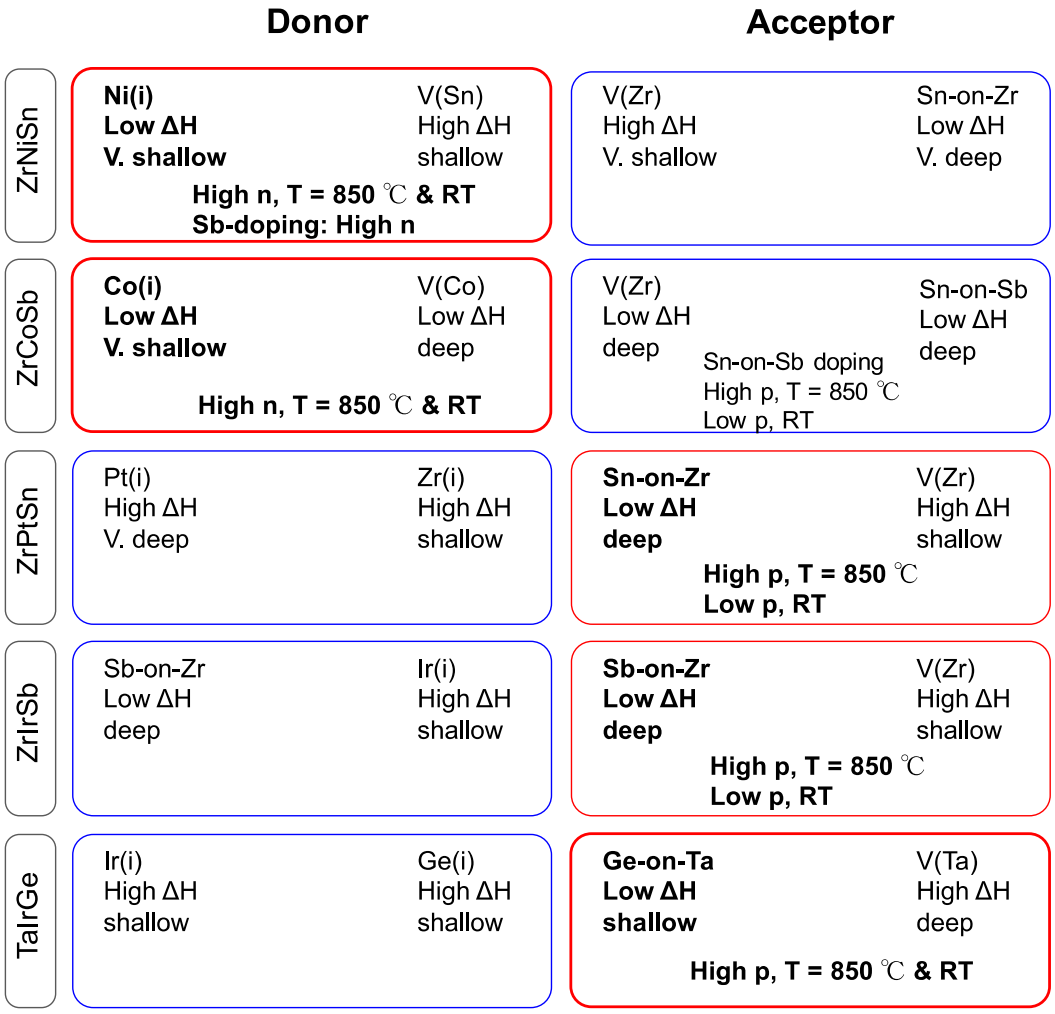

FIG. 11. *Summary of doping trends in five ABC compounds (ZrNiSn, ZrCoSb, ZrPtSn, ZrIrSb, and TaIrGe).* For each system we show the dominant donors (red frame) and dominant acceptors (blue frame), indicating for each defect if its formation energy at equilibrium Fermi level is 'high' as well as if the transition level is shallow (i.e its carrier-producing) or deep (i.e, carriers are not released). Dominant (high density) defects are shown in bold face. We used the following notation: 'V. shallow' stands for 'very shallow'; 'high n' and 'high p' denote 'high *n*-type density' and 'high *p*-type density', respectively.

APPENDIX: TECHNICAL DETAILS AND SUPPORTING INFORMATION ON THIS CARRIER DOPING STUDY

Bulk compounds and their properties

Table 1. Fundamental electronic band gaps of the $A^{IV}NiSn$, $A^{IV}PtSn$, $A^{IV}CoSb$, and $A^{IV}IrSb$ groups (A=Ti, Zr, and Hf) half-Heusler compounds using hybrid functional calculations (HSE) [60,70,71]. All HSE fundamental gaps are of the Γ-X indirect character, except HfIrSb which has a direct gap (see band structures in Fig. 13). The lattice constant was relaxed by the GGA+U method.

Compound	a_0 (Å)	E_g [HSE] (eV)	Experimental carrier types
TiNiSn	5.95	0.60	n [37,43,65,72]
ZrNiSn	6.19	0.55	n [43]
HfNiSn	6.16	0.45	n [22]
TiPtSn	6.23	1.31	n/p [69]
ZrPtSn	6.44	1.28	**p** [69]
HfPtSn	6.41	1.20	**p** [69]
TiCoSb	5.90	1.42	n [34,38]
ZrCoSb	6.13	1.49	n [34]
HfCoSb	6.10	1.41	n [34]
TiIrSb	6.38	1.70	
ZrIrSb	6.35	2.06	**p** [13]
HfIrSb	6.18	1.57	

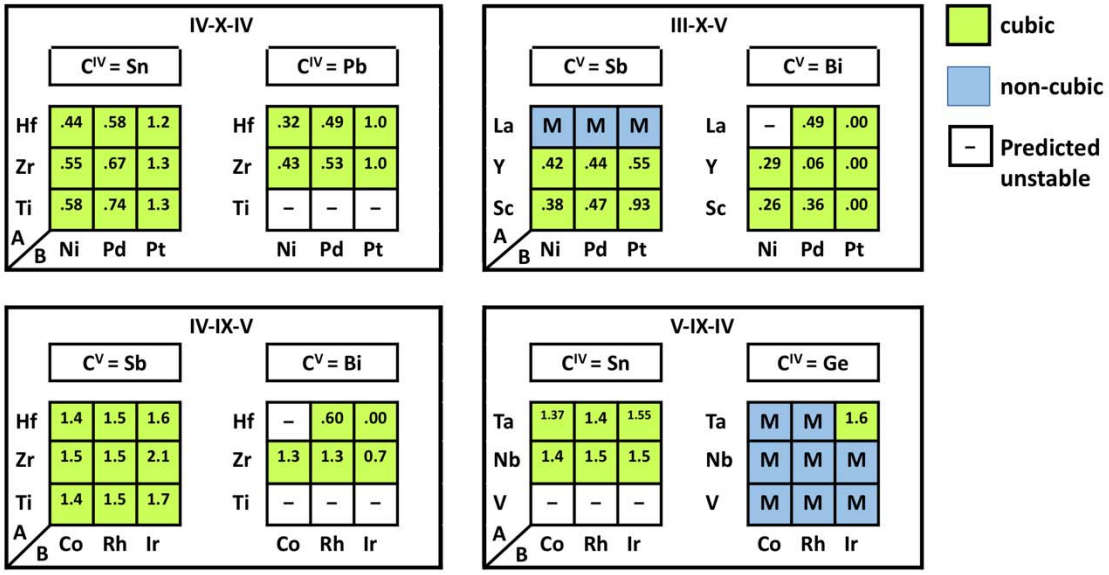

FIG. 12. Fundamental band gaps (in eV, from HSE calculation) of a group of 18-valence-electron half-Heusler compounds in four prototype chemical groups $A^{IV}B^{X}C^{IV}$, $A^{IV}B^{IX}C^{V}$, $A^{III}B^{X}C^{V}$, and $A^{V}B^{IX}C^{IV}$. The ternary compounds with cubic structure (F $\bar{4}$3m) are non-metal (shaded in green), whereas those in non-cubic structures are metal (shaded in blue). Those that are predicted unstable are denoted by minus sign (–).

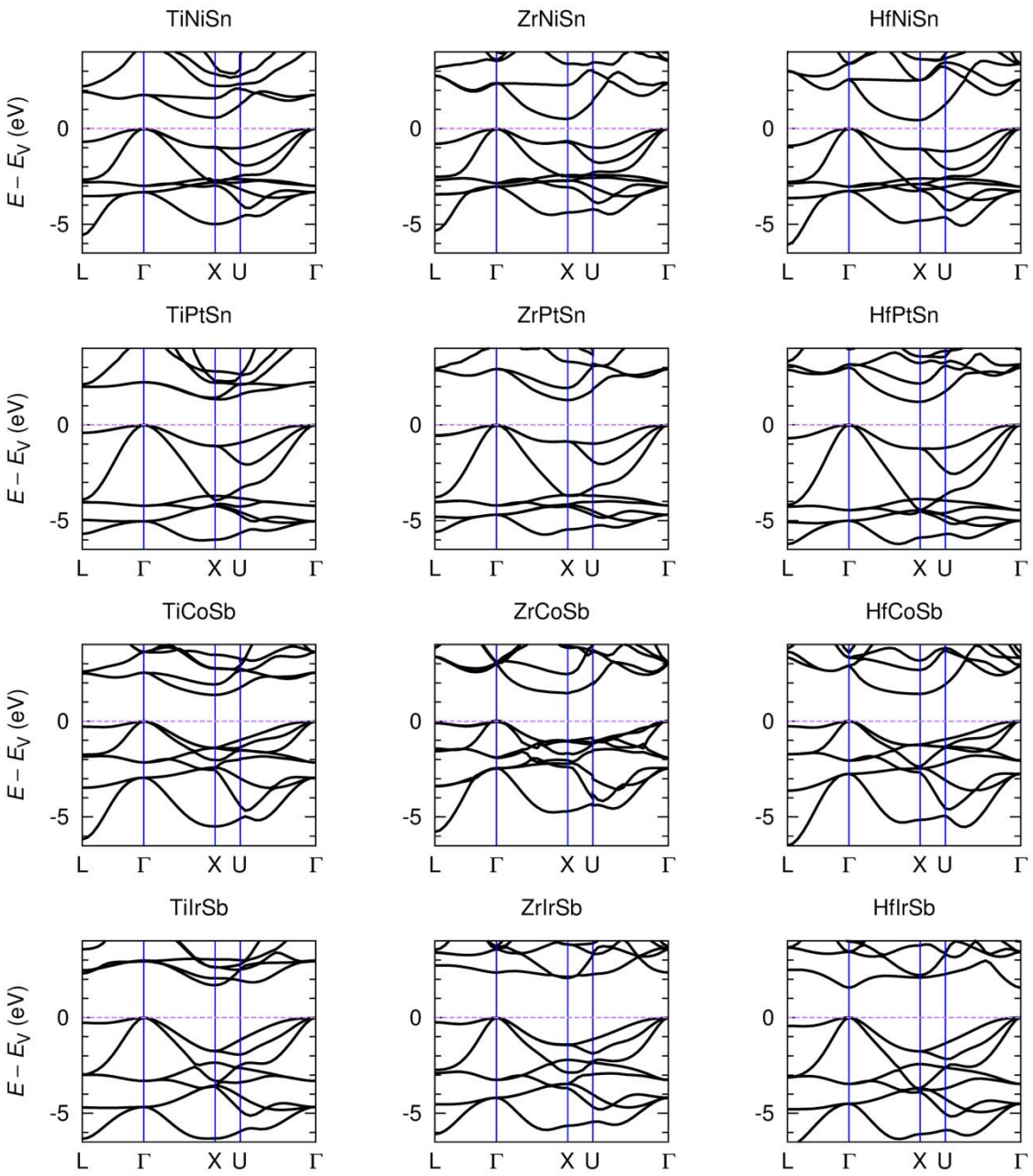

FIG. 13. Electronic band structure of the twelve half-Heusler compounds from hybrid functional calculations (HSE). The energy (eigenvalue) reference is set to E_V, the valence band maximum.

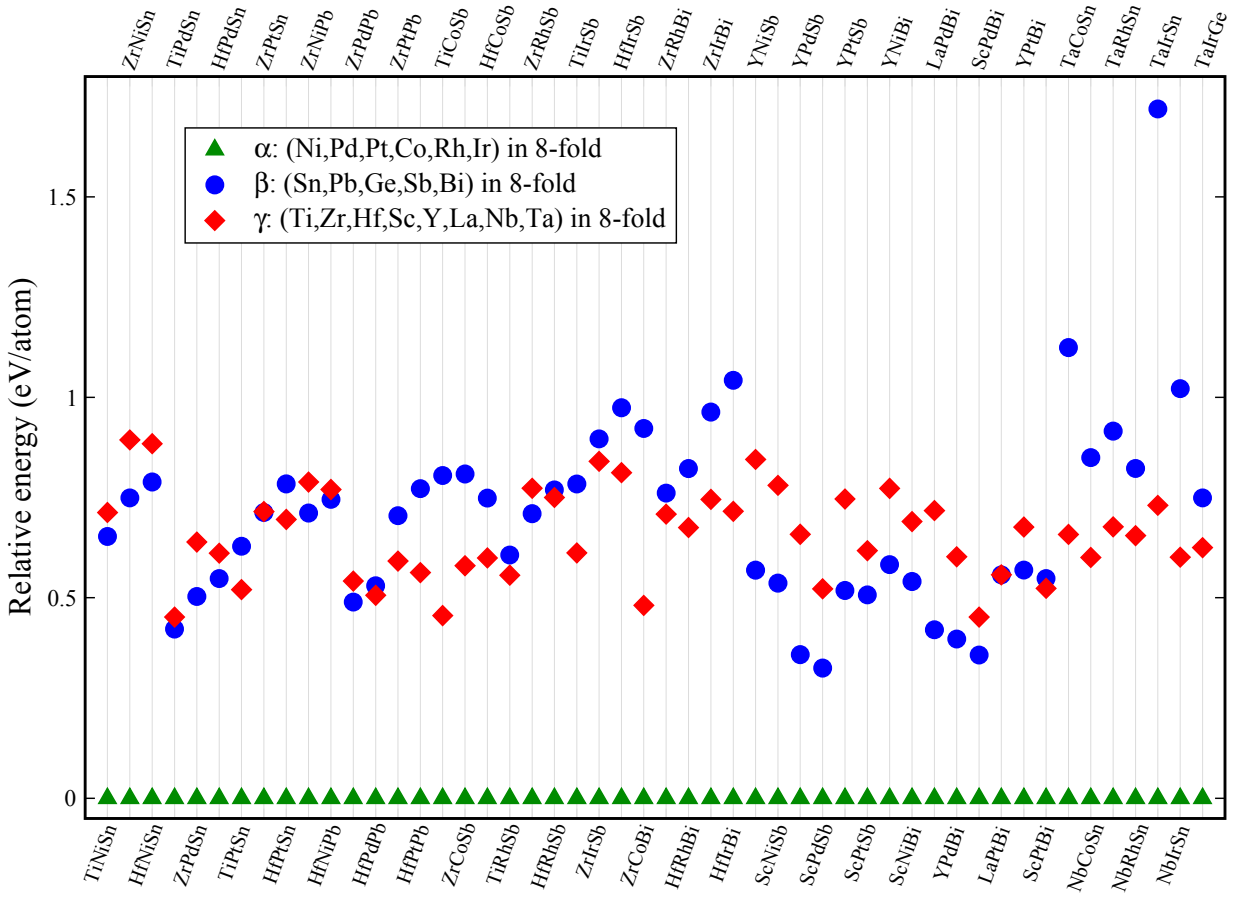

FIG. 14. Relative total energies (eV per atom) of the β and γ structures of the ABC compounds with respect to the ground state α phase for the fifty cubic ABC half-Heusler compounds from Fig. 1. In α structure, the group VIII elements (Ni, Pd, Pt, Co, Rh, Ir) occupy 8-fold site and the other two elements occupy the two 4-fold sites (see Fig. 2a); in β structure, the group IVA and VA elements (Sn, Pb, Ge, Sb, Bi) occupy 8-fold site; in γ structure, the group IIIB, IVB, VB elements (Ti, Zr, Hf, Sc, Y, La, Nb, Ta) occupy 8-fold site. In all cases the ground state is the α phase.

Compound formation enthalpies and competing phases

Table 2. Competing phases used for defining the chemical stability diagrams of ZrNiSn, ZrCoSb, ZrPtSn, ZrIrSb and TaIrGe. A more thorough list of competing phases can be found in Table S2 in Ref. [14] for TaIrGe.

ABX Compound	ZrNiSn	ZrCoSb	ZrPtSn	ZrIrSb	TaIrGe
Competing phases	Zr_3Sn Zr_5Sn_3 Zr_5Sn_4 NiSn Ni_3Sn Ni_3Sn_2 Ni_3Sn_4 NiZr Ni_2Zr Ni_3Zr Ni_5Zr $ZrNi_2Sn$ $ZrNi_4Sn$ Zr_2Ni_2Sn	ZrSb $ZrSb_2$ Zr_2Sb Zr_3Sb Zr_5Sb_3 Zr_5Sb_4 CoSb $CoSb_2$ $CoSb_3$ ZrCo $ZrCo_2$ Zr_2Co Zr_3Co	Zr_5Sn_3 Zr_5Sn_4 PtSn $PtSn_2$ $PtSn_4$ Pt_2Sn_3 Pt_3Sn ZrPt $ZrPt_3$ Zr_5Pt_3 Zr_9Pt_{11}	ZrSb $ZrSb_2$ Zr_2Sb Zr_3Sb Zr_5Sb_3 Zr_5Sb_4 IrSb $IrSb_2$ $IrSb_3$ ZrIr Zr_2Ir $ZrIr_2$ $ZrIr_3$ Zr_3Ir Zr_5Ir_3 Zr_6IrSb_2	Ta_3Ge Ta_5Ge_3 $TaGe_2$ IrGe $IrGe_4$ Ir_4Ge_5 Ir_3Ge_7 TaIr $TaIr_3$

Table 3. Calculated formation enthalpies in unit of eV per atom of five half-Heusler FTS (ZrNiSn, ZrCoSb, ZrPtSn, ZrIrSb, and TaIrGe) and their major competing phases. The DFT calculations were performed with the GGA+U method, except for those denoted by star (*), where plain GGA was used. The DFT+FERE method (see computational details in the next section) is applies only to the GGA+U results [73]. Calculations were compared to calorimetry data from [74-76].

(a) Five half-Heusler materials

Half-Heusler materials	ΔH_f (eV/atom) DFT	ΔH_f (eV/atom) DFT+FERE	ΔH_f (eV/atom) Exp.
ZrNiSn	-0.656	-0.943	
ZrCoSb	-0.615	-0.773	
ZrPtSn	-1.032	-1.153	
ZrIrSb	-0.962	-1.082	
TaIrGe	-0.668	-0.750	

(b) Competing phases for ZrNiSn

Compounds	ΔH_f (eV/atom) DFT	ΔH_f (eV/atom) DFT+FERE	ΔH_f (eV/atom) Exp.
Zr_3Sn	-0.289	-0.850	
Zr_5Sn_3	-0.552	-1.026	-0.738
Zr_5Sn_4	-0.557	-0.982	
NiSn	-0.269	-0.332	
Ni_3Sn	-0.193	-0.271	-0.253
Ni_3Sn_2	-0.284	-0.353	-0.301
Ni_3Sn_4	-0.246	-0.306	-0.308
NiZr*	-0.452		-0.523
Ni_2Zr*	-0.410		
Ni_3Zr*	-0.463		
Ni_5Zr*	-0.326		
$ZrNi_2Sn$	-0.517	-0.755	
$ZrNi_4Sn$	-0.350	-0.540	
Zr_2Ni_2Sn	-0.564	-0.902	

(c) Competing phases for ZrCoSb

Compounds	ΔH_f (eV/atom) DFT	ΔH_f (eV/atom) DFT+FERE	ΔH_f (eV/atom) Exp.
ZrSb	-0.695	-0.977	
$ZrSb_2$	-0.534	-0.665	-0.902
Zr_2Sb	-0.589	-1.022	-1.043
Zr_3Sb	-0.489	-0.998	-0.83
Zr_5Sb_3	-0.617	-1.012	-1.116
Zr_5Sb_4	-0.624	-0.957	
CoSb*	-0.164		-0.197
$CoSb_2$*	-0.106		-0.176
$CoSb_3$*	-0.142		-0.166
ZrCo*	-0.291		-0.37
$ZrCo_2$*	-0.311		-0.371
Zr_2Co*	-0.254		-0.274
Zr_3Co*	-0.200		

(d) Competing phases for ZrPtSn

Compounds	ΔH_f (eV/atom) DFT	ΔH_f (eV/atom) DFT+FERE	ΔH_f (eV/atom) Exp.
Zr_5Sn_3	-0.552	-1.026	-0.738
Zr_5Sn_4	-0.557	-0.982	
PtSn*	-0.646		-0.609
$PtSn_2$*	-0.481		-0.542
$PtSn_4$*	-0.295		-0.282
Pt_2Sn_3*	-0.553		-0.564
Pt_3Sn*	-0.469		-0.52
ZrPt*	-1.084		-1.078
$ZrPt_3$*	-1.017		
Zr_5Pt_3*	-0.813		
Zr_9Pt_{11}*	-0.784		

(e) Competing phases for ZrIrSb

Compounds	ΔH_f (eV/atom) DFT	ΔH_f (eV/atom) DFT+FERE	ΔH_f (eV/atom) Exp.
ZrSb	-0.695	-0.977	
$ZrSb_2$	-0.534	-0.665	-0.902
Zr_2Sb	-0.589	-1.022	-1.043
Zr_3Sb	-0.489	-0.998	-0.83
Zr_5Sb_3	-0.617	-1.012	-1.116
Zr_5Sb_4	-0.624	-0.957	
IrSb	-0.322	-0.142	-0.206
$IrSb_2$	-0.438	-0.261	-0.151
$IrSb_3$	-0.398	-0.222	-0.114
ZrIr*	-0.770		-0.888
Zr_2Ir*	-0.651		
$ZrIr_2$*	-0.674		
$ZrIr_3$*	-0.703		
Zr_3Ir*	-0.512		
Zr_5Ir_3*	-0.719		
Zr_6IrSb_2*	-1.115		

(f) Competing phases for TaIrGe

Compounds	ΔH_f (eV/atom) DFT	ΔH_f (eV/atom) DFT+FERE	ΔH_f (eV/atom) Exp.
Ta_3Ge	-0.306	-0.599	
Ta_5Ge_3	-0.284	-0.532	
$TaGe_2$	-0.209	-0.352	
IrGe	-0.426	-0.343	
$IrGe_4$	-0.196	-0.176	
Ir_4Ge_5	-0.427	-0.356	
Ir_3Ge_7	-0.299	-0.258	
TaIr*	-0.587		
$TaIr_3$*	-0.682		

(g) Summary of the FERE correction to GGA+U formation enthalpies when comparison with experimental data is available [74-76].

Compounds	ΔH_f (eV/atom) DFT	ΔH_f (eV/atom) DFT+FERE	ΔH_f (eV/atom) Exp.
Ni_3Sn	-0.193	-0.271	-0.253
Ni_3Sn_2	-0.284	-0.353	-0.301
Ni_3Sn_4	-0.246	-0.306	-0.308
Zr_5Sn_3	-0.552	-1.026	-0.738
$ZrSb_2$	-0.534	-0.665	-0.902
Zr_2Sb	-0.589	-1.022	-1.043
Zr_3Sb	-0.489	-0.998	-0.830
Zr_5Sb_3	-0.617	-1.012	-1.116
Zr_5Sn_3	-0.552	-1.026	-0.738
IrSb	-0.322	-0.142	-0.206
$IrSb_2$	-0.438	-0.261	-0.151
$IrSb_3$	-0.398	-0.222	-0.114

Concept and computational formula for defects and doping

Defect formation energy is defined as the energy cost to create a point charged defect in an infinite lattice space (i.e. at dilute limit) through exchanging atom and electron with chemical reservoir and Fermi Sea, respectively. To extract the defect formation energy from a finite supercell calculation, one uses the following formula

$$\Delta H(D,q,\mu_\alpha,E_F) = \{E(D,q) - E_H\} \pm \sum_\alpha(\mu_\alpha^0 + \Delta\mu_\alpha) + q(E_V + E_F) + \delta H_{\rm corr} \quad (1),$$

where $\Delta H(D,q,\mu_\alpha,E_F)$ is the formation energy of defect D in charge state q under the condition of elemental chemical potential μ_α and the parametric electronic Fermi energy E_F (relative to the valence band maximum E_V). $E(D, q)$ is the energy of the supercell containing defect D in charge state q, and E_H is the energy of the host; μ_α is the chemical potential of atoms in the reservoir, which can be decomposed into values for pure elements (μ_α^0) and the excess chemical potential ($\Delta\mu_\alpha$). We will provide in the following section specific details on the method of calculation, the way finite cell size and DFT errors are rectified to obtain $\delta H_{\rm corr}$ the correction to the defect formation energy, and explain how relaxation is taken into account (see for example [52,77,78]).

Charge transition level of a specific defect is defined as the Fermi energy $E_{\rm F}^*$, at which two charged states q and q' have equal formation energy $\Delta H(D,q,\mu_\alpha,E_{\rm F}^*) = \Delta H(D,q',\mu_\alpha,E_{\rm F}^*)$, which has been calculated from Eq. (1). This gives

$$E_{\rm F}^* = \varepsilon(D,q|q') = \frac{\{E(D,q)+\delta H_{\rm corr}(D,q)\}-\{E(D,q')+\delta H_{\rm corr}(D,q')\}}{q'-q} - E_V. \quad (2)$$

The transition levels are an intrinsic property for the defect and do not depend on chemical potential.

Equilibrium Fermi level can explicitly determine how much carriers can be doped into the compounds. Enforcing the charge neutrality condition, we have

$$\sum_{s=1}^{\rm nsite} n_s \sum_{D,q} q_{s,(D,q)} \frac{1}{Z_s} \exp\left(-\beta\Delta H_{form}(D,q,\{\mu_\alpha\},E_F)\right) = \int_{E_{\rm C}}^{\infty} g(E) f_{\rm FD}(E) dE - \int_{-\infty}^{E_{\rm V}} g(E)(1 - f_{\rm FD}(E)) dE \quad (3)$$

Here E_F is an input continuous formal parameter used to scan $\Delta H(D, q, \mu_\alpha, E_F)$ when VBM < E_F < CBM, whereas $\boldsymbol{E_F^{eq}}$ is the thermodynamic equilibrium Fermi energy obtained as the output solution. In specific, Z_s is the partition function on site s due to all charge defects competing with the ordered host, i.e. $Tr(-\beta\Delta H_{\rm form})$ with $\beta = 1/k_B T$; $g(E)$ is the electronic density of state and f_{FD} is the Fermi-Dirac distribution; $\{\mu_\alpha\}$ is the set of chemical potential under which $\Delta H_{\rm form}$ is defined; n_s is degeneracy of site s per unit cell. $g(E)$ is the density of states obtained from DFT calculation of the host compound and fitted by cubic spline for an interpolation at the logarithmic energy grid. Clearly equilibrium E_F depends on chemical potentials and *temperat*ure. Figure 21 gives an example of the calculated equilibrium Fermi energy as a function of chemical potential and growth temperature.

Defect concentration and carrier density: Once $E_F^{eq}(T, \{\mu_\alpha\})$ is obtained self-consistently in Eq. 3, the concentration of each charged defect (D, q) is obtained as they are the weighted Boltzmann value on the left hand side of Eq. 3.

Computational detail for defects and doping

Calculating the $E(D, q) - E_H$ term: The calculation of the $E(D, q) - E_H$ terms needs to benefit as much as possible from cancelation of errors . Therefore, both quantities need to be calculated at equivalent K point set, basis set size and other integration grids. We use a bcc-type rhombohedral supercell containing 48 atoms; increasing the supercell dimension to a $2 \times 2 \times 2$ cubic cell containing 96 atoms has small effects as illustrated in Fig. 15. For the cut-off energy for the plane wave basis set we use 1.3 times the maximum default cutoff from each pseudopotential in an ABC compound (360 eV maximum). To compute E(D, q) and E_H we use the pseudopotential total energy and force formalism, the Perdew-Burke-Ernzerhof (PBE) GGA functional and the PAW-PBE pseudopotential approach, as implemented in the VASP code [79-81].

Post processor corrections: The $\delta H_{\rm corr}$ term expresses the 'post-processor' corrections, which is necessary to deal with two classes of errors (a) the finite supercell effects and (b) DFT errors. (We

emphasize that calculations that omit some of these corrections can err by 0.5–1 eV). The spurious effects (a) introduced from periodic images of the single defect include the following. (i) The fact that the supercell is generally of order ~100 atoms or less and contains at least one defect implies a potentially unrealistically high concentration of carriers that would fill the conduction or valence band if the underlying defects have delocalized wavefunctions. This is the well-known Moss-Burstein band-filling effect for impurities in semiconductors. The band-filling *correction* works by replacing the interacting band dispersion due to shallow defect by an eigen state at CBM (donor case) or VBM (acceptor case) [82,83]. (ii) The total energy formula for charged periodic system includes an arbitrary constant. To address this, the consistency between the defect system and the host system far away from the defect site requires aligning their electrostatic potential at a position in the defect cell that has minimal effects from the defect. The energy variation associated with this electrostatic potential shift ($q(V[D,q]-V[host])$) is the potential alignment correction. (iii) The spurious interaction between charges in different supercells distorts the results due to finite size effects. The image charge correction [84] eliminates the spurious Coulomb interaction arising from such periodic image charges, for which we use the method of Lany and Zunger [52].

The second class of corrections (b) pertains to the fact that irrespective of supercell size, DFT functionals, such as LDA or GGA, are known to introduce errors in band edges of the host compound and in the defect eigenstates. These entail specific post processor corrections described in Ref [52]. In the current paper we use the hybrid functional (HSE) method [60,70,71] that performs rather well in terms of band gaps, so the class of corrections (b) is not needed in this case. Figure 15 describes the defect levels and defect formation energy in HSE as well as uncorrected GGA+U in two supercell sizes. The conspicuous difference between HSE and GGA results lies in charge transition levels. For instance, ZrNiSn is the small band gap insulator (E_g= 0.55 eV), posing difficulties for GGA to predict eigenvalues for in-gap states due to the lack of non-local exchange effect in GGA. The GGA functional wrongly predicted that Ni interstitial cannot ionize (Fig. 15), hence the carrier density in ZrNiSn will be exceptional low (~10^{14} cm^{-3}) even if the total interstitial defect concentration is significant (10^{21} cm^{-3}), which contradicts the high *n*-type carrier density found in experiment. In HSE study, the Ni_i is a shallow donor, ready to ionize and release carriers. Therefore, HSE is adopted in this defect study. The effect of increasing the supercell size from bcc-rhombohedron shape (48-atom) to simple cubic (96 atoms) on defect formation energy is rather minor (Fig. 15), since the separation between the nearest periodic

images in the two cases are already large, 10.7 Å and 12.4 Å, respectively, and supercell correction is very helpful, although there exist small differences in transition levels of V_{Zr} and V_{Sn} from HSE calculations using the two supercells (Fig. 15).

Calculating compound formation enthalpies and chemical potentials: Regarding formation energies of compounds and the related chemical potentials, we calculated the excess chemical potential diagrams using the formation enthalpies of each compound and its competing phases at the DFT-GGA+U level. Systematic DFT errors in formation energies of compounds were systematically corrected using the fitted elementary reference energy method (FERE[73]) in which the chemical potential of elemental phases (such as solid A or molecular C) obtained from GGA+U were shifted so that the calculated compound formation energies are fitted to the experimental data for a large set of binary and ternary compounds. The FERE-corrected GGA+U formation energy substantially improves the agreement with calorimetry data, especially for the Ni-Sn, Zr-Sb, Zr-Ir binary compounds (Table 3; Note that calorimetry data for ABC ternary compounds are rare.) For metal alloys and compounds we use the plain GGA results rather than GGA+U, as the use of U is not well justified in such systems. Comparison with experiment on metal alloys is also encouraging, e.g. in Pt-Sn and Zr-Co system as well as for ZrIr and ZrPt (Table 3). Further attempt using higher level functionals such as HSE was deemed unnecessary.

Atomic displacements and relaxation: To compute the local atomic displacements in each charge state, we start by introducing random displacements to the first nearest neighbor atoms around the defect site and assigned a magnetic moment of 0.7 μ_B to the impurity atom to account for initial spin polarization. This step is needed to avoid locking of the displacement or magnetism at a local minima characterizing the ideal cubic structure. Then, all internal atomic positions are relaxed using the GGA+U method without any symmetry constraint until each component of the residual force was within 5×10^{-3} eV/Å. Using the fixed cell geometry obtained from GGA+U, we then evaluated the total energy of the defect system by the hybrid functional method that included nonlocal exchange.

Stability and convergence of defect computational scheme

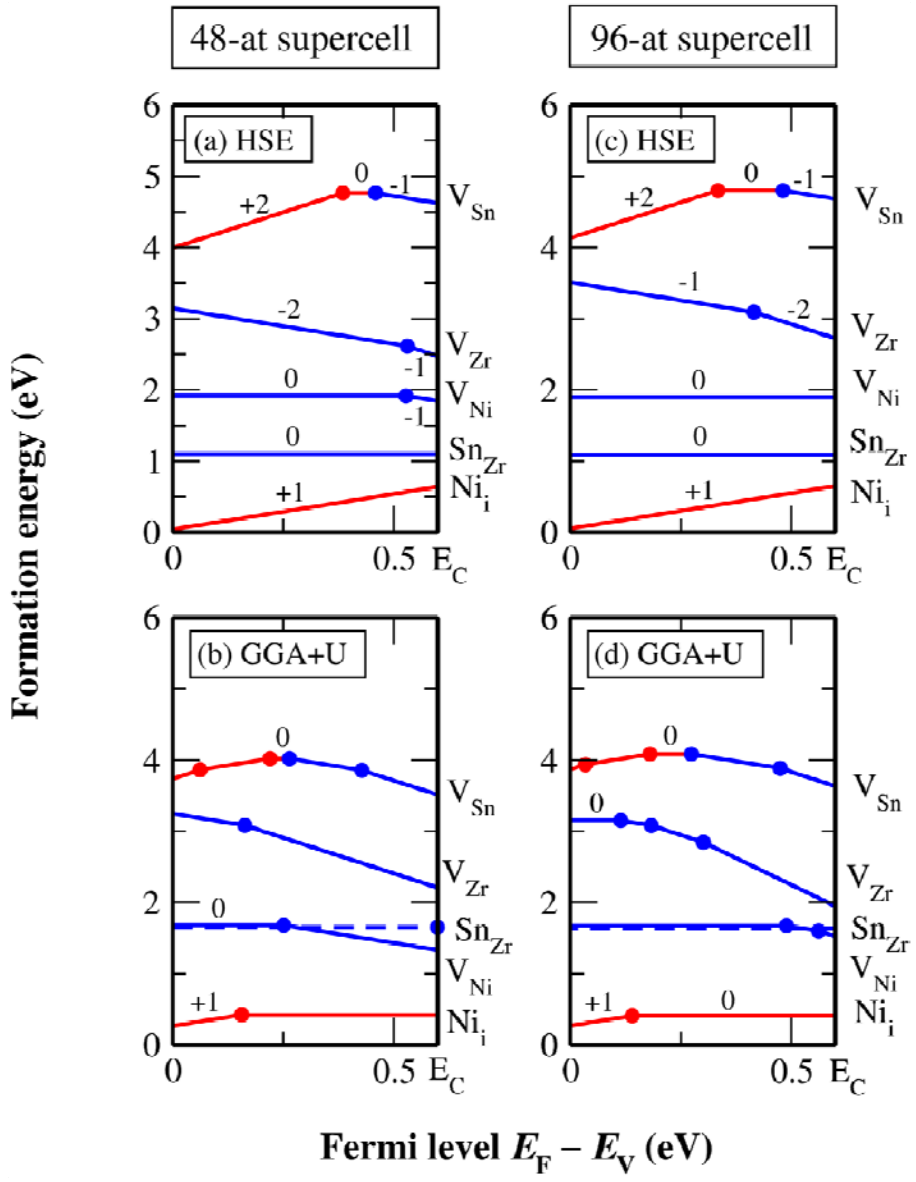

FIG. 15. Supercell size dependence of the HSE and GGA+U defect formation energies in ZrNiSn.

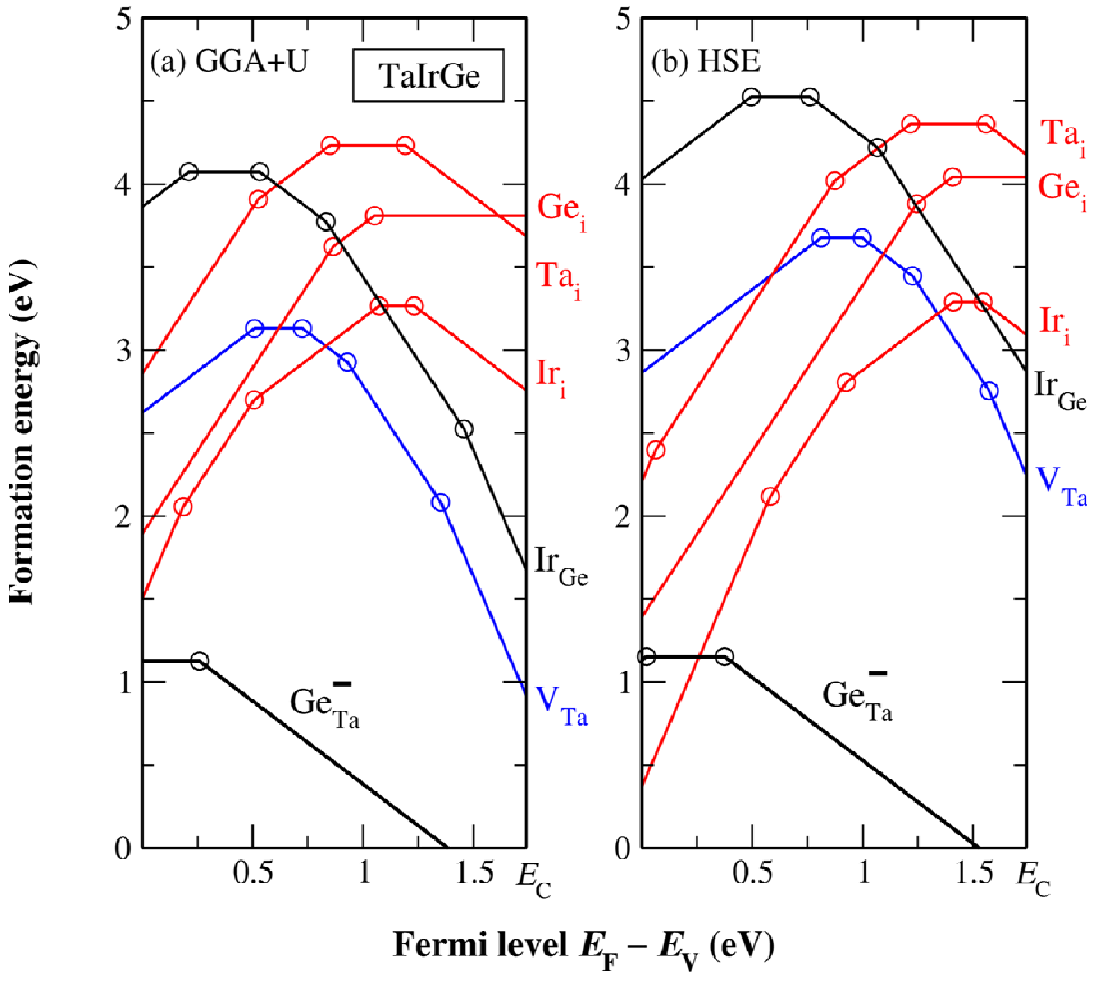

FIG. 16. Comparison between GGA+U and HSE study on formation energy of intrinsic defects in TaIrGe at the Ge-rich and Ta-poor condition in a 48-atom supercell. The computed equilibrium *p*-type carrier concentration is cm^{-3} in GGA+U and cm^{-3} by HSE.

$ZrNi_{1+x}Sn$: band gaps and thermodynamics of mixing properties

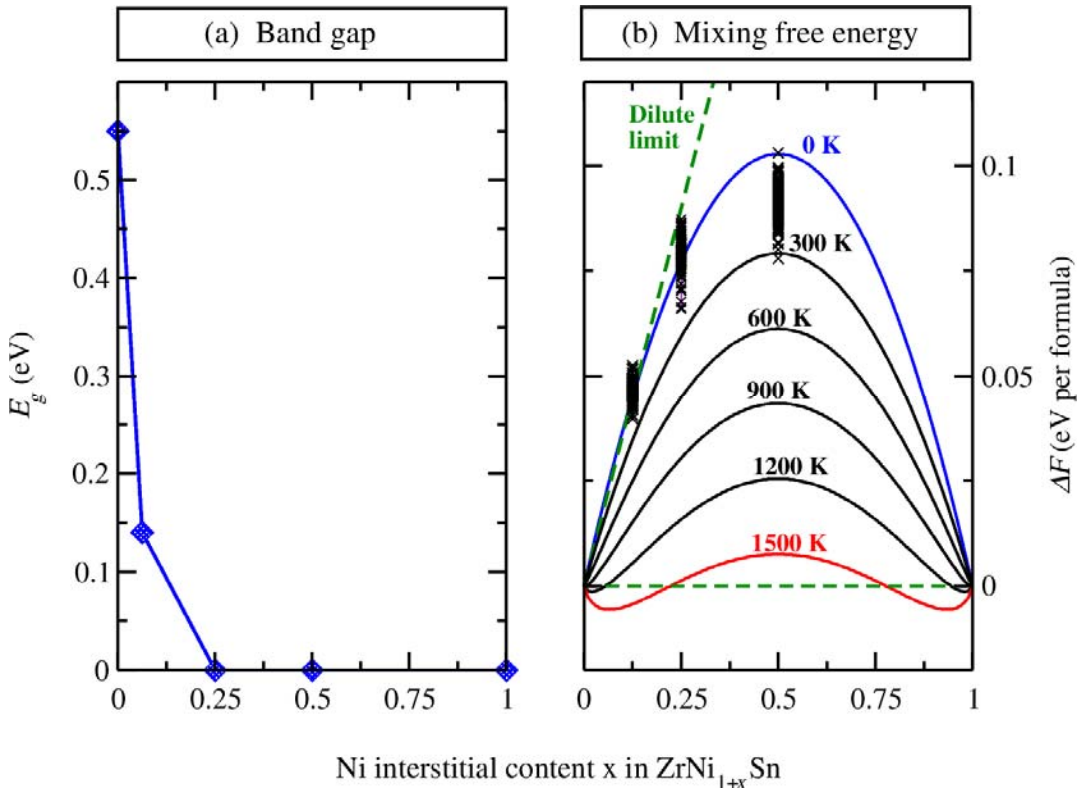

Fig. 17. Electronic band gap of $ZrNi_{1+x}Sn$ from HSE study using a few configurations (a), and the temperature dependence of the mixing Helmholtz free energy vs Ni interstitial content x in $ZrNi_{1+x}Sn$ assuming a regular solid solution behavior: , with w being the Margules parameter for enthalpy of mixing, fitted to configurations within a supercell (b).

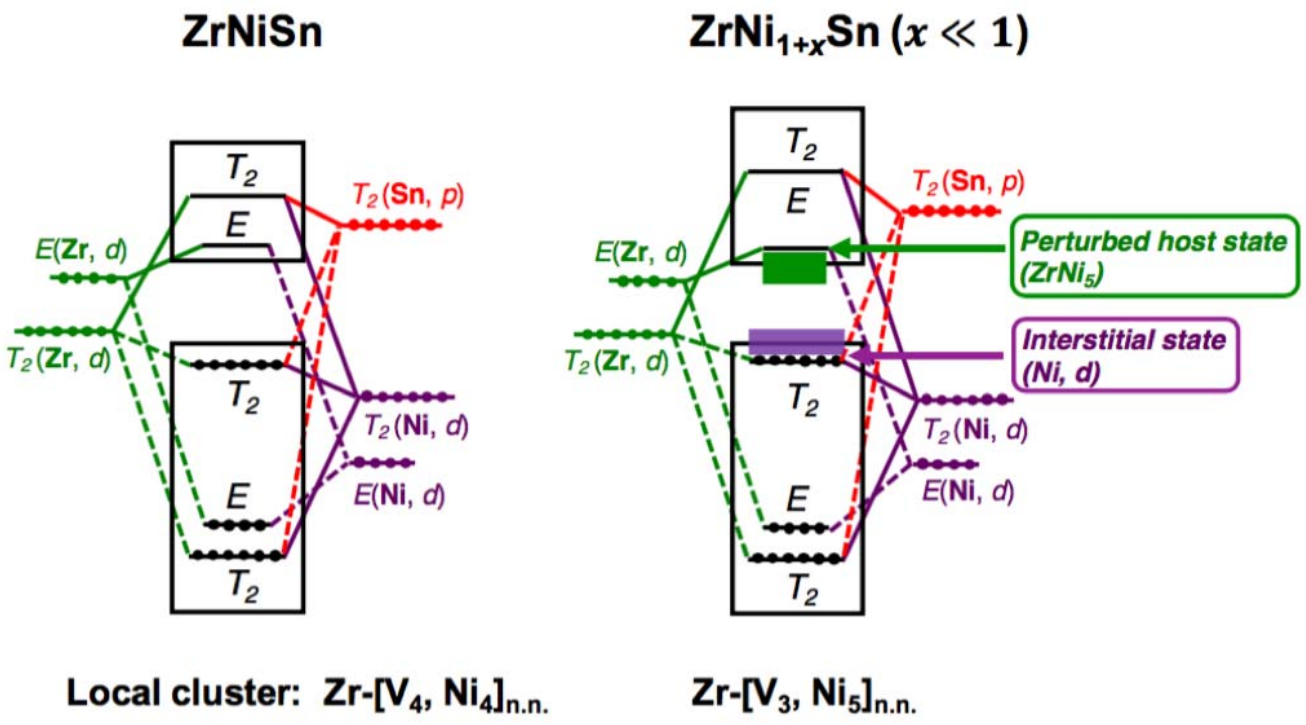

FIG. 18. Evolution of the orbital diagram from ZrNiSn to $ZrNi_{1+x}Sn$ ( ), inducing the band gap reduction due to the formation of perturbed host state (from a local $ZrNi_5$ cluster) near conduction band minimum and the Ni interstitial states near the edge of the valence band maximum.

Frenkel defects in ZrNiSn

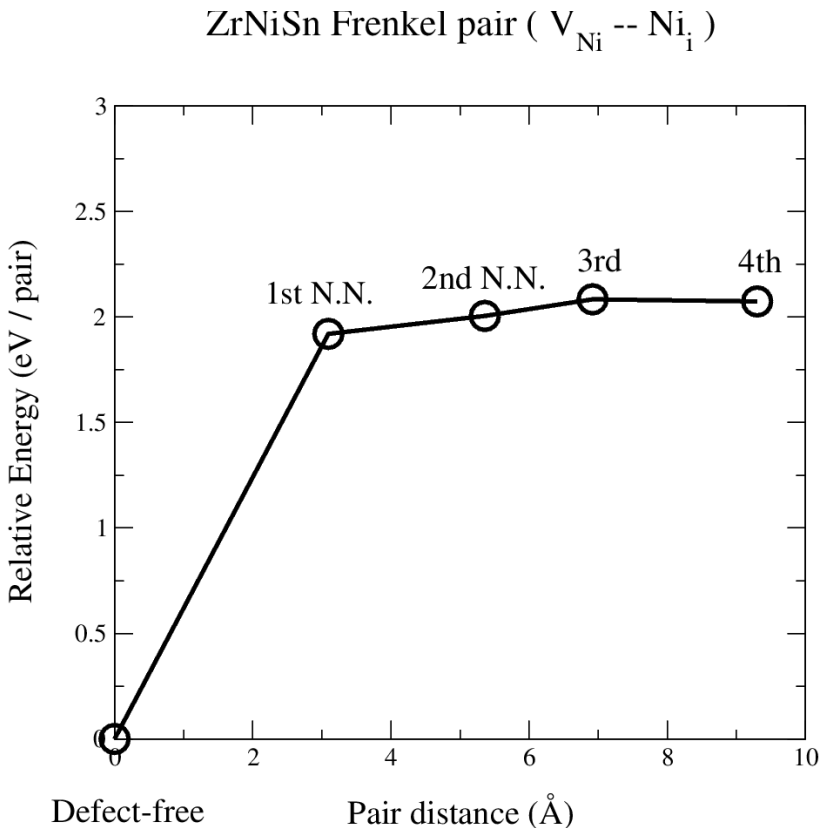

FIG. 19. Energetics of a Frenkel pair (Ni interstitial plus Ni vacancy) relative to the defect free host state as a function of the pair distance in a ZrNiSn supercell.

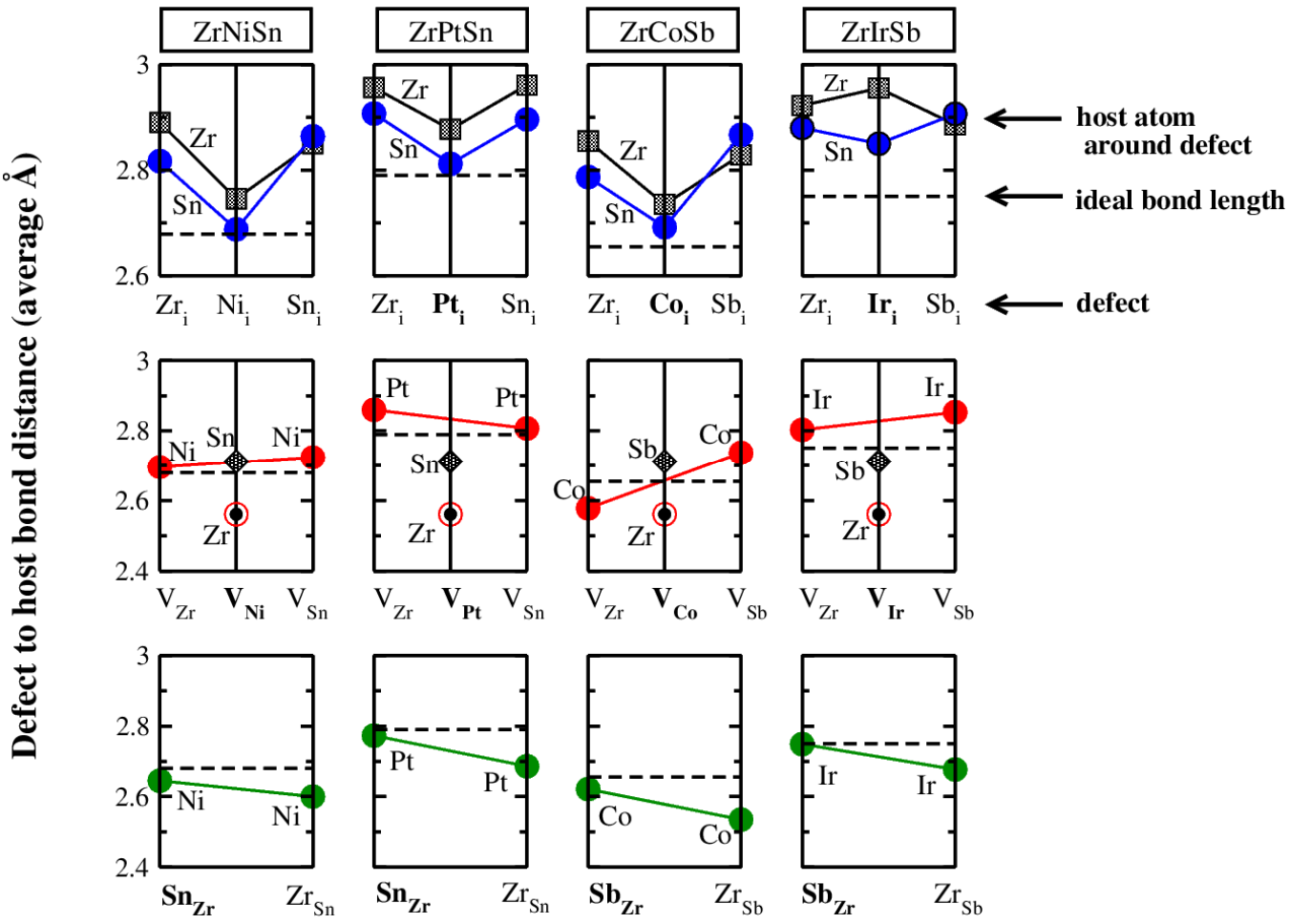

FIG. 20. The averaged first nearest neighbor bond distances from the defect centers to their surrounding host atoms — the bond lengths around the three interstitials: Zr_i, Ni_i, Sn_i (top row), three vacancies V_{Zr}, V_{Ni}, V_{Sn} (middle), and the two antisite defects: Sn_{Zr} and Zr_{Sn} (bottom).

Equilibrium Fermi level, carrier density, and charged defect concentration versus chemical potential conditions

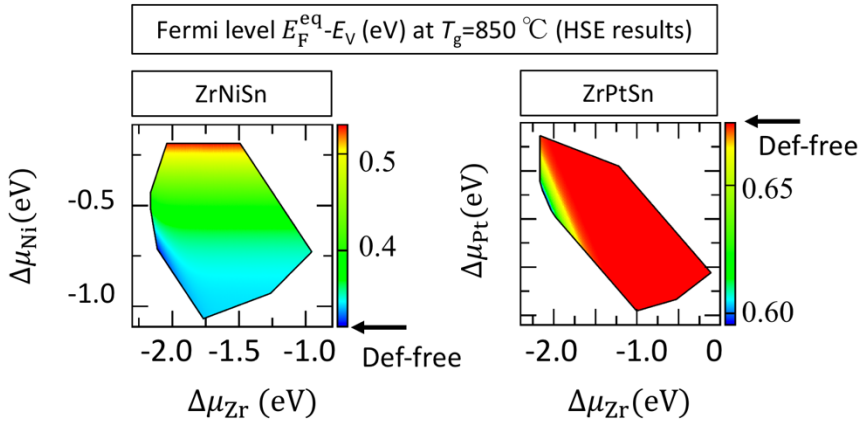

FIG. 21. The equilibrium Fermi level relative to the valence band maximum at growth condition for the two ABC half-Heusler compounds due to self-doping mechanism arising from intrinsic defects: *n*-type ZrNiSn and *p*-type ZrPtSn. It is the self-consistent solution to the charge neutrality condition (Eq. 3 in Appendix). Please note that the Fermi level in defect-free compounds are at E_V + 0.33 and E_V + 0.67 eV, respectively, for ZrNiSn and ZrPtSn. The fundamental (-X) band gaps of ZrNiSn and ZrPtSn are 0.55 and 1.28 eV, respectively (HSE results).

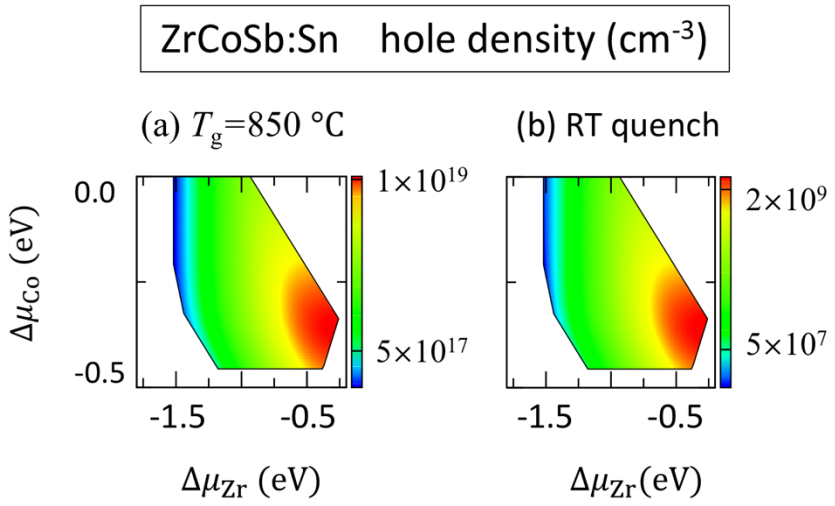

FIG. 22. The majority (hole) carrier density in Sn-doped ZrCoSb as a function of excess chemical potential conditions at (a) growth condition (T_g=850 °C) and (b) room temperature from quench after growth.

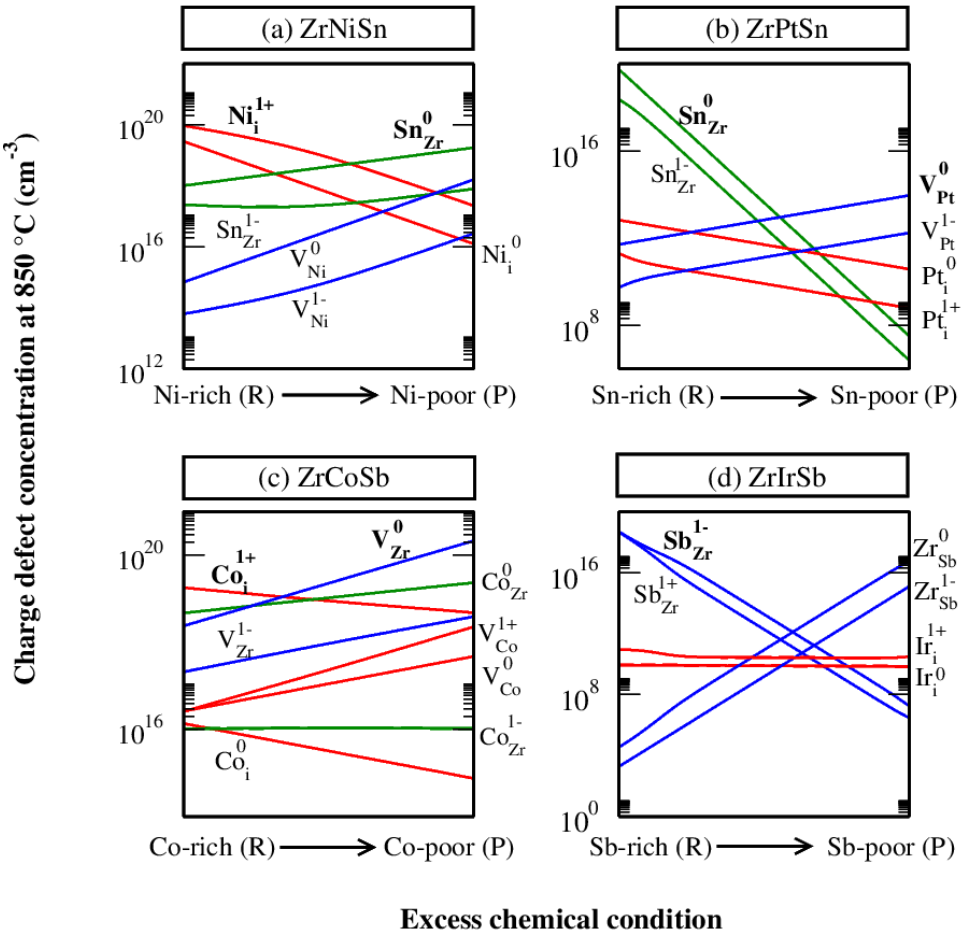

FIG. 23. Variation of dominant charged impurity concentrations in representative half-Heusler compounds at growth condition (T_g=850 °C) along a line of chemical potential conditions (R–P) connecting the rich and poor chemical potential conditions as shown in Fig. 9. The red, blue, and green colors denote interstitial, vacancy, and antisite defects, respectively.

Reference

[1] E. Parthe, *Crystal Chemistry of Tetrahedral Structures* (Gordon and Breach Science Publishers, New York, 1964).
[2] L. I. Berger, *Semiconductor Materials* (CRC Press, Boca Raton, Florida, 1996).
[3] H. Nowotny and W. Siebert, Zeit Met. **33**, 391 (1941).
[4] H. Nowotny and K. Bachmayer, Monatshefte Für Chem. Verwandte Teile Anderer Wiss. **81**, 488 (1950).
[5] R. Juza and F. Hund, Z. Für Anorg. Chem. **257**, 1 (1948).
[6] R. Juza and F. Hund, Naturwissenschaften **33**, 121 (1946).
[7] D. M. Wood, A. Zunger, and R. de Groot, Phys Rev B **31**, 2570 (1985).
[8] A. E. Carlsson, A. Zunger, and D. M. Wood, Phys Rev B **32**, 1386 (1985).
[9] S.-H. Wei and A. Zunger, Phys Rev Lett **56**, 528 (1986).
[10] F. Casper, T. Graf, S. Chadov, B. Balke, and C. Felser, Semiconductor Science and Technology **27**, 063001 (2012).
[11] F. Casper, R. Seshadri, and C. Felser, Phys Status Solidi A **206**, 1090 (2009).
[12] X. W. Zhang, L. P. Yu, A. Zakutayev, and A. Zunger, Adv Funct Mater **22**, 1425 (2012).
[13] R. Gautier, X. W. Zhang, L. H. Hu, L. P. Yu, Y. Y. Lin, T. O. L. Sunde, D. Chon, K. R. Poeppelmeier, and A. Zunger, Nat Chem **7**, 308 (2015).
[14] F. Yan, X. W. Zhang, Y. G. Yu, L. P. Yu, A. Nagaraja, T. O. Mason, and A. Zunger, Nat Commun **6** (2015).
[15] *ICSD, Inorganic Crystal Structure Database* (Fachinformationszentrum Karlsruhe, Karlsruhe, Germany 2013).
[16] S. Chadov, X. Qi, J. Kubler, G. H. Fecher, C. Felser, and S. C. Zhang, Nature materials **9**, 541 (2010).
[17] H. Lin, L. A. Wray, Y. Xia, S. Xu, S. Jia, R. J. Cava, A. Bansil, and M. Z. Hasan, Nature materials **9**, 546 (2010).
[18] A. Roy, J. W. Bennett, K. M. Rabe, and D. Vanderbilt, Phys Rev Lett **109**, 037602 (2012).
[19] S. Wang, Z. Wang, W. Setyawan, N. Mingo, and S. Curtarolo, Physical Review X **1**, 021012 (2011).
[20] G. J. Snyder and E. S. Toberer, Nature materials **7**, 105 (2008).
[21] G. J. Snyder and T. S. Ursell, Phys Rev Lett **91**, 148301 (2003).
[22] C. Uher, J. Yang, S. Hu, D. T. Morelli, and G. P. Meisner, Phys Rev B **59**, 8615 (1999).
[23] K. Ishizaka *et al.*, Nature materials **10**, 521 (2011).
[24] J. Kübler, A. R. William, and C. B. Sommers, Phys Rev B **28**, 1745 (1983).
[25] R. A. de Groot, F. M. Mueller, P. G. van Engen, and K. H. J. Buschow, Phys Rev Lett **50**, 2024 (1983).
[26] N. P. Butch, P. Syers, K. Kirshenbaum, A. P. Hope, and J. Paglione, Phys Rev B **84**, 220504 (2011).
[27] W. Al-Sawai, H. Lin, R. S. Markiewicz, L. A. Wray, Y. Xia, S. Y. Xu, M. Z. Hasan, and A. Bansil, Phys Rev B **82**, 125208 (2010).
[28] G. Trimarchi, X. Zhang, M. J. DeVries Vermeer, J. Cantwell, K. R. Poeppelmeier, and A. Zunger, Phys Rev B **92**, 165103 (2015).
[29] M. J. D. Vermeer, X. Zhang, G. Trimarchi, M. D. Donakowski, P. J. Chupas, K. R. Poeppelmeier, and A. Zunger, J Am Chem Soc **137**, 11383 (2015).

[30] A. Zakutayev, X. Zhang, A. Nagaraja, L. Yu, S. Lany, T. O. Mason, D. S. Ginley, and A. Zunger, J Am Chem Soc **135**, 10048 (2013).
[31] S. V. Dudiy and A. Zunger, Phys Rev Lett **97**, 046401 (2006).
[32] A. Franceschetti, S. V. Dudiy, S. V. Barabash, A. Zunger, J. Xu, and M. van Schilfgaarde, Phys Rev Lett **97**, 047202 (2006).
[33] A. Franceschetti and A. Zunger, Nature **402**, 60 (1999).
[34] Y. Xia, V. Ponnambalam, S. Bhattacharya, A. L. Pope, S. J. Poon, and T. M. Tritt, Journal of Physics: Condensed Matter **13**, 77 (2001).
[35] J. P. Heremans, V. Jovovic, E. S. Toberer, A. Saramat, K. Kurosaki, A. Charoenphakdee, S. Yamanaka, and G. J. Snyder, Science (New York, N.Y.) **321**, 554 (2008).
[36] R. S. M. Wambach, S. Bhattacharya, P. Ziolkowski, E. Müller, G.K.H. Madsen, A. Ludwig, Advanced Electronic Materials **2**, 1500208 (2016).
[37] J. E. Douglas, C. S. Birkel, M.-S. Miao, C. J. Torbet, G. D. Stucky, T. M. Pollock, and R. Seshadri, Applied Physics Letters **101**, 183902 (2012).
[38] J. K. Kawasaki, L. I. M. Johansson, B. D. Schultz, and C. J. Palmstrøm, Applied Physics Letters **104**, 022109 (2014).
[39] Y. Pei, A. F. May, and G. J. Snyder, Advanced Energy Materials **1**, 291 (2011).
[40] Y. V. Stadnyk, V. A. Romaka, Y. K. Gorelenko, L. P. Romaka, D. Fruchart, and V. F. Chekurin, Journal of Alloys and Compounds **400**, 29 (2005).
[41] Heinrich Hohl, Art P. Ramirez, Claudia Goldmann, Gabriele Ernst, Bernd Wölfing, and E. Bucher, Journal of Physics: Condensed Matter **11**, 1697 (1999).
[42] T. Wu, W. Jiang, X. Li, Y. Zhou, and L. Chen, Journal of Applied Physics **102**, 103705 (2007).
[43] H. Xie, H. Wang, C. Fu, Y. Liu, G. J. Snyder, X. Zhao, and T. Zhu, Scientific Reports **4**, 6888 (2014).
[44] V. V. Romaka, P. Rogl, L. Romaka, Y. Stadnyk, A. Grytsiv, O. Lakh, and V. Krayovskii, Intermetallics **35**, 45 (2013).
[45] A. Zunger, Applied Physics Letters **83**, 57 (2003).
[46] J. P. Perdew and A. Zunger, Phys Rev B **23**, 5048 (1981).
[47] J. Schmitt, Z. M. Gibbs, G. J. Snyder, and C. Felser, Materials Horizons **2**, 68 (2015).
[48] F. G. Aliev, N. B. Brandt, V. V. Kozyrkov, V. V. Moshchalkov, R. V. Skolozdra, Y. V. Stadnyk, and V. K. Pecharskii, Jetp Lett. **45**, 684 (1987).
[49] S. Öğüt and K. M. Rabe, Phys Rev B **51**, 10443 (1995).
[50] P. Qiu, J. Yang, X. Huang, X. Chen, and L. Chen, Applied Physics Letters **96**, 152105 (2010).
[51] P. Larson, S. D. Mahanti, and M. G. Kanatzidis, Phys Rev B **62**, 12754 (2000).
[52] S. Lany and A. Zunger, Phys Rev B **78**, 235104 (2008).
[53] P. R. C. Kent and A. Zunger, Phys Rev Lett **86**, 2613 (2001).
[54] Dat T. Do, S D Mahanti, and J. J. Pulikkoti, Journal of Physics: Condensed Matter **26**, 275501 (2014).
[55] Koji Miyamoto *et al.*, Applied Physics Express **1**, 081901 (2008).
[56] V. A. Romaka, P. Rogl, V. V. Romaka, Y. V. Stadnyk, E. K. Hlil, V. Y. Krajovskii, and A. M. Horyn, Semiconductors **47**, 892 (2013).
[57] R. Shan, E. V. Vilanova, J. Qin, F. Casper, G. H. Fecher, G. Jakob, and C. Felser, physica status solidi (RRL) – Rapid Research Letters **7**, 145 (2013).
[58] K. Mastronardi, D. Young, C.-C. Wang, P. Khalifah, R. J. Cava, and A. P. Ramirez, Applied Physics Letters **74**, 1415 (1999).
[59] T. Sekimoto, K. Kurosaki, H. Muta, and S. Yamanaka, Materials Transactions **48**, 2079 (2007).

[60] J. Heyd, G. E. Scuseria, and M. Ernzerhof, The Journal of Chemical Physics **118**, 8207 (2003).
[61] J. Buckeridge, D. O. Scanlon, A. Walsh, and C. R. A. Catlow, Computer Physics Communications **185**, 330 (2014).
[62] K. Irmscher, M. Naumann, M. Pietsch, Z. Galazka, R. Uecker, T. Schulz, R. Schewski, M. Albrecht, and R. Fornari, physica status solidi (a) **211**, 54 (2014).
[63] F. J. Manjón, M. Mollar, M. A. Hernández-Fenollosa, B. Marí, R. Lauck, and M. Cardona, Solid State Communications **128**, 35 (2003).
[64] J. D. Perkins *et al.*, Phys Rev B **84**, 205207 (2011).
[65] S. Bhattacharya, A. L. Pope, R. T. Littleton, T. M. Tritt, V. Ponnambalam, Y. Xia, and S. J. Poon, Applied Physics Letters **77**, 2476 (2000).
[66] J. E. Douglas, C. S. Birkel, N. Verma, V. M. Miller, M.-S. Miao, G. D. Stucky, T. M. Pollock, and R. Seshadri, Journal of Applied Physics **115**, 043720 (2014).
[67] J. Osorio-Guillén, S. Lany, S. V. Barabash, and A. Zunger, Phys Rev B **75**, 184421 (2007).
[68] P. Qiu, X. Huang, X. Chen, and L. Chen, Journal of Applied Physics **106**, 103703 (2009).
[69] Y. Kimura, A. Zama, and Y. Mishima, in *2006 25th International Conference on Thermoelectrics*2006), pp. 115.
[70] J. Heyd, G. E. Scuseria, and M. Ernzerhof, The Journal of Chemical Physics **124**, 219906 (2006).
[71] J. Heyd and G. E. Scuseria, J Chem Phys **121**, 1187 (2004).
[72] Y. W. Chai and Y. Kimura, Acta Materialia **61**, 6684 (2013).
[73] V. Stevanovic, S. Lany, X. W. Zhang, and A. Zunger, Phys Rev B **85** (2012).
[74] W. E. Liu and S. E. Mohney, Materials Science and Engineering: B **103**, 189 (2003).
[75] S. V. Meschel and O. J. Kleppa, Thermochimica Acta **314**, 205 (1998).
[76] L. Topor and O. J. Kleppa, Metallurgical Transactions A **19**, 1827 (1988).
[77] L. Stephan and Z. Alex, Modelling and Simulation in Materials Science and Engineering **17**, 084002 (2009).
[78] C. Freysoldt, B. Grabowski, T. Hickel, J. Neugebauer, G. Kresse, A. Janotti, and C. G. Van de Walle, Reviews of Modern Physics **86**, 253 (2014).
[79] J. Ihm, A. Zunger, and M. L. Cohen, Journal of Physics C: Solid State Physics **12**, 4409 (1979).
[80] G. Kresse and J. Hafner, Phys Rev B **47**, 558 (1993).
[81] G. Kresse and J. Furthmüller, Computational Materials Science **6**, 15 (1996).
[82] T. S. Moss, Proceedings of the Physical Society. Section B **67**, 775 (1954).
[83] E. Burstein, Physical Review **93**, 632 (1954).
[84] G. Makov and M. C. Payne, Phys Rev B **51**, 4014 (1995).